

Structures of the interleukin 11 signalling complex reveal gp130 dynamics and the inhibitory mechanism of a cytokine variant

Received: 31 October 2022

Accepted: 20 October 2023

Published online: 20 November 2023

 Check for updates

Riley D. Metcalfe^{1,7,9}, Eric Hanssen^{1,2,3,9}, Ka Yee Fung^{4,5}, Kaheina Aizel^{1,4,5}, Clara C. Kosasih^{1,4,5}, Courtney O. Zlatich¹, Larissa Doughty¹, Craig J. Morton^{1,8}, Andrew P. Leis^{2,4,5}, Michael W. Parker^{1,3,6}, Paul R. Gooley¹, Tracy L. Putoczki^{4,5,10} & Michael D. W. Griffin^{1,3,10} ✉

Interleukin (IL)-11, an IL-6 family cytokine, has pivotal roles in autoimmune diseases, fibrotic complications, and solid cancers. Despite intense therapeutic targeting efforts, structural understanding of IL-11 signalling and mechanistic insights into current inhibitors are lacking. Here we present cryo-EM and crystal structures of the human IL-11 signalling complex, including the complex containing the complete extracellular domains of the shared IL-6 family β -receptor, gp130. We show that complex formation requires conformational reorganisation of IL-11 and that the membrane-proximal domains of gp130 are dynamic. We demonstrate that the cytokine mutant, IL-11 Mutein, competitively inhibits signalling in human cell lines. Structural shifts in IL-11 Mutein underlie inhibition by altering cytokine binding interactions at all three receptor-engaging sites and abrogating the final gp130 binding step. Our results reveal the structural basis of IL-11 signalling, define the molecular mechanisms of an inhibitor, and advance understanding of gp130-containing receptor complexes, with potential applications in therapeutic development.

Interleukin (IL)-11 is secreted by numerous immune cells including CD8⁺ T-cells, B-cells, macrophages, natural killer (NK) cells, $\gamma\delta$ T cells, and eosinophils, and has been implicated in the differentiation of B-cells, T-cells, and anti-tumour immune responses^{1–5}. IL-11 is also produced by inflammatory fibroblasts and epithelial cells resulting in a coordinated wound response to enable the maintenance of mucosal barriers^{6–11}. It is now appreciated that the biological function of IL-11 spans beyond its classical role in megakaryocytopoiesis^{12,13}, where recombinant IL-11 (Neumega) is FDA approved to support platelet

reconstitution following chemotherapy¹⁴. Critical pathological roles for dysregulated IL-11 have been identified in autoimmune diseases including arthritis, asthma, inflammatory bowel disease, multiple sclerosis, and systemic sclerosis^{3,4,6,7,15,16}. In addition, IL-11 drives fibrotic complications of the gastrointestinal tract, heart, kidney, liver and lung^{6,9–11,17–20}, and promotes the growth of several malignancies, including breast, lung, endometrial and gastrointestinal cancers^{21–25}. Despite these physiological and pathological roles, structural understanding of IL-11 signalling has remained limited.

¹Department of Biochemistry and Pharmacology, Bio21 Molecular Science and Biotechnology Institute, University of Melbourne, Parkville, Victoria 3010, Australia. ²Ian Holmes Imaging Centre, Bio21 Molecular Science and Biotechnology Institute, University of Melbourne, Parkville, Victoria 3010, Australia. ³ARC Centre for Cryo-electron Microscopy of Membrane Proteins, Bio21 Molecular Science and Biotechnology Institute, University of Melbourne, Parkville, Victoria 3010, Australia. ⁴Walter and Eliza Hall Institute of Medical Research, Parkville, Victoria 3052, Australia. ⁵Department of Medical Biology, University of Melbourne, Parkville, Victoria 3010, Australia. ⁶St Vincent's Institute of Medical Research, Fitzroy, Victoria 3065, Australia. ⁷Present address: Center for Structural Biology, Center for Cancer Research, National Cancer Institute, Frederick, Maryland 21702, USA. ⁸Present address: CSIRO Biomedical Manufacturing Program, Clayton, Victoria 3168, Australia. ⁹These authors contributed equally: Riley D. Metcalfe, Eric Hanssen. ¹⁰These authors jointly supervised this work: Tracy L. Putoczki, Michael D. W. Griffin. ✉e-mail: mgriffin@unimelb.edu.au

IL-11 activates downstream signalling pathways by binding its two cell surface receptors: the IL-11 specific receptor, IL-11R α , and the signal-transducing receptor, glycoprotein (gp)130^{13,26}. Following the formation of the receptor complex, the Janus kinase (JAK)/signal transducer and activator of stat (STAT) and extracellular signal regulated kinase (ERK)/mitogen-activated protein kinase (MAPK) pathways are primarily activated^{13,27–29}. IL-11 is a member of the IL-6 family of cytokines, which also includes IL-6, IL-27, IL-31, IL-35, IL-39 leukaemia inhibitory factor (LIF), oncostatin M (OSM), ciliary neurotrophic factor (CNTF), cardiotrophin-1 (CT-1), cardiotrophin-like cytokine factor 1 (CLCF1), and an analogue of IL-6 from human herpes virus 8 (vIL-6)^{30–32}. The IL-6 family is commonly defined by the shared use of gp130, and thus overlaps with the IL-12 family³³. IL-11 and IL-6 utilise a homodimer of gp130^{26,34,35} while other IL-6 family members exploit a heterodimer of gp130 with a second signal-transducing receptor, such as LIF receptor (LIFR), OSM receptor (OSMR), IL-27R/WSX-1 or IL-12 receptor β -2 subunit (IL-12R β 2)³⁶. IL-31 is unique in its use of the gp130-like receptor chain, IL-31RA, and OSMR. gp130 is a member of the tall type-I cytokine receptor family, with a large extracellular region comprising six domains, D1–D6²⁷. Crystal structures of IL-6³⁷, vIL-6³⁴, LIF³⁷ and IL-27^{38,39} in complex with D1–D3 of gp130, in addition to cryo-EM structures of CNTF, CLCF1, LIF, IL-27, and IL-6 in complex with their receptor ectodomains⁴⁰, show that the membrane distal domains are involved in cytokine binding. However, the nature of the membrane proximal D4–D6 domains of gp130 within cytokine-receptor complexes has not been fully elucidated⁴⁰.

Inhibition of IL-11 signalling has been shown to provide therapeutic benefit in models of arthritis, multiple sclerosis, neointimal hyperplasia, multiple fibrotic diseases, and gastrointestinal cancers^{9–11,13,17,20,21,24,41,42}. Current IL-11 signalling inhibitors include IL-11 mutants^{43,44} and antibodies against either IL-11^{9,20,45} or IL-11R α ^{11,46–48}. However, mechanistic understanding of their modes of action is limited in the absence of detailed molecular understanding of the IL-11 signalling complex. Informed development of new and existing signalling inhibitors requires a comprehensive understanding of the structure and assembly mechanisms of the IL-11 signalling complex.

Here, we present structures of the human IL-11 signalling complex, providing detail of the molecular mechanisms of complex formation and the structure and dynamics of the complete extracellular domains of gp130 within the complex. We characterise an IL-11 variant, IL-11 Mutein, that potently inhibits IL-11 signalling and describe the detailed mechanism of its action. Our results validate IL-11 Mutein as a tool to inhibit IL-11 signalling and provide a straightforward method for its production. Our insights reveal the structural basis of IL-11 signalling and provide invaluable molecular platforms for development of existing and novel therapeutics targeting IL-11 signalling and other class I cytokines.

Results

The structure of the IL-11 signalling complex

To understand the molecular mechanisms underpinning human IL-11 signalling complex formation, we solved three structures of the complex (Fig. 1) containing either the cytokine binding domains of gp130 (gp130_{D1–D3}) or the complete extracellular domains of gp130 (gp130_{EC}) using electron cryo-microscopy (cryo-EM) and X-ray crystallography. Complexes included an N-terminally truncated form of IL-11 (IL-11 Δ ₁₀) or full-length IL-11 (IL-11_{FL}), and a C-terminally truncated form of IL-11R α (IL-11R α _{D1–D3}) or the complete extracellular domains of IL-11R α (IL-11R α _{EC}) described previously⁴⁹.

We obtained a 3.5 Å resolution cryo-EM reconstruction of the IL-11 Δ ₁₀/IL-11R α _{D1–D3}/gp130_{D1–D3} complex (referred to as the gp130_{D1–D3} complex) (Fig. 1Ai; Supplementary Fig. 1A; Supplementary Fig. 2A, B; Supplementary Table 1), and a 3.8 Å resolution cryo-EM reconstruction of the IL-11 Δ ₁₀/IL-11R α _{D1–D3}/gp130_{EC} complex (referred to as the gp130_{EC} complex) (Fig. 1Bi, Supplementary Fig. 1B; Supplementary

Fig. 2C, D; Supplementary Table 1). We used these data to build and refine the atomic models of the IL-11 signalling complex (Fig. 1Aii, Bii). We also obtained crystals of the IL-11_{FL}/IL-11R α _{EC}/gp130_{D1–D3} complex that diffracted anisotropically to 3.8 Å. We used the cryo-EM structure of the gp130_{D1–D3} complex to phase the X-ray diffraction data by molecular replacement (Fig. 1C). Three IL-11 signalling complexes were arranged in a triangular configuration in the asymmetric unit providing 6-fold non-crystallographic symmetry to aid refinement (Supplementary Fig. 3A–C).

Secondary structure was clearly visible in both cryo-EM density maps, larger side chains were generally defined, the α -helical structure of the cytokine was clear, and β -strands were generally separated, consistent with maps reconstructed at these resolutions (Supplementary Fig. 2B, D). D1 of IL-11R α was not visible in the gp130_{D1–D3} complex map and was poorly defined in the gp130_{EC} complex map (Supplementary Fig. 2Di), suggesting this domain is flexible. Satisfactory density defining the positions of the β -sheets of IL-11R α D1 facilitated refinement of the domain in the gp130_{EC} complex and the crystal structure, confirming the average positions of this domain in the complex (Supplementary Fig. 2Di; Supplementary Fig. 3). N-linked glycans were visible on IL-11R α (N105, N172) and gp130 (N21, N61, N135) in all structures (Supplementary Fig. 4). D5–D6 of gp130 were poorly defined in the gp130_{EC} complex density (Fig. 1Bi) and were not included in the deposited model. However, density was sufficient to refine the positions of these domains as rigid bodies (shown in grey in Fig. 1Bii).

All structures show a hexamer consisting of two copies each of IL-11, IL-11R α and gp130, in agreement with previous immunoprecipitation and native-gel electrophoresis experiments²⁶, and a low-resolution EM map of the complex³⁰. The structures bear a striking resemblance to a table, with D2 of IL-11R α and gp130, and IL-11 forming the table-top, and D3 of IL-11R α and gp130 forming the legs (Fig. 1Aii), similar to the IL-6³⁵ and vIL-6³⁴ complexes. The density for the gp130_{EC} complex shows that D5–D6 of the two gp130 molecules cross over (Fig. 1Bii), as previously suggested by low-resolution EM reconstructions of the complete extracellular domains of the IL-6^{51,52} and IL-11⁵⁰ signalling complexes, and recent cryo-EM studies of the IL-6 signalling complex⁴⁰.

Sedimentation velocity analytical ultracentrifugation (SV-AUC) provided sedimentation coefficient distributions with single, narrow peaks for the gp130_{D1–D3} and gp130_{EC} complexes at 7.1 S and 8.4 S, respectively (Fig. 1D). Molecular masses for the gp130_{D1–D3} and gp130_{EC} complexes estimated from SV-AUC of 178.7 kDa (frictional ratio [f/f_0]: 1.6) and 269.4 kDa (f/f_0 : 1.8) were consistent with masses calculated from sequence (169.8 kDa and 235.0 kDa) as were masses determined by multi-angle light scattering (MALS) of M_w : 187.3 kDa and M_w : 259.6 kDa (Supplementary Fig. 5A). Higher experimental masses than those calculated from sequence are likely due to N-linked glycans present on the receptors.

To confirm the solution stoichiometry, we used sedimentation equilibrium analytical ultracentrifugation (SE-AUC), which provides a relative molecular mass (M^*) for the complex and its components independent of the extent of glycosylation. SE-AUC of the gp130_{D1–D3} and gp130_{EC} complexes yielded M^* of 176.5 kDa and 255.5 kDa respectively (Supplementary Fig. 5C–E), in excellent agreement with the sum of the M^* values obtained for the hexamer components of 179.2 kDa and 264.4 kDa.

To further probe the solution configuration of the hexamer we collected small-angle X-ray scattering (SAXS) data for the gp130_{D1–D3} and gp130_{EC} complexes (Fig. 1E; Supplementary Fig. 6A–D; Supplementary Table 3). Our atomic coordinates fit the scattering data well (Fig. 1E, Supplementary Table 3), and masses derived from the data of 182.2 kDa and 290.0 kDa agree with calculated hexamer masses. Deviations of the theoretical scattering profile from the experimental data at high q may be due to truncated N-linked glycans in the

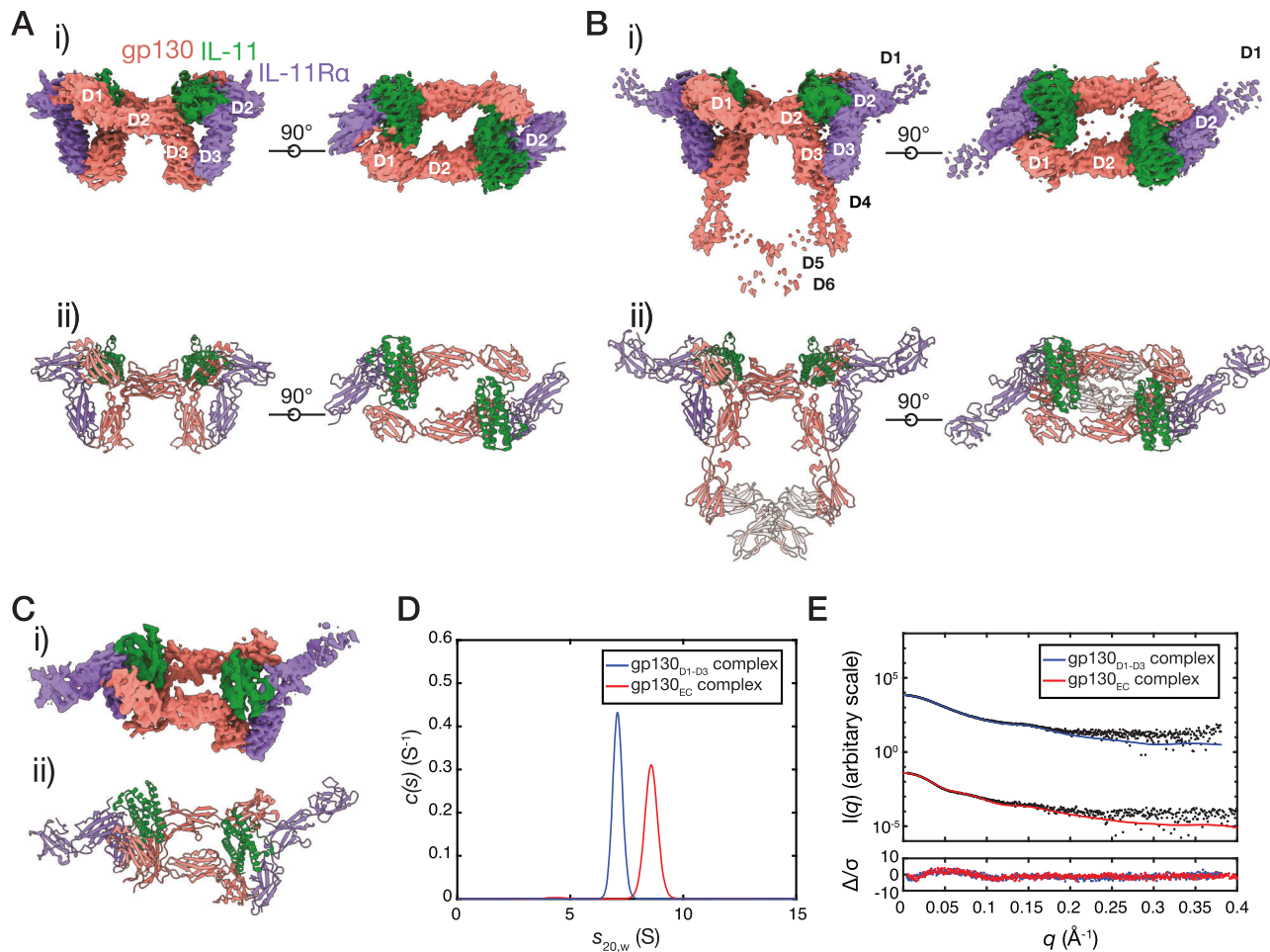


Fig. 1 | Structure of the IL-11 signalling complex (IL-11, green; IL-11R α , purple; gp130 salmon). **A** Cryo-EM density map (contoured at 7σ), (i), and atomic model, (ii), of the IL-11 Δ_{10} /IL-11R α_{D1-D3} /gp130 $_{D1-D3}$ complex. D1 of IL-11R α was not modelled in this structure. **B** Cryo-EM density map (contoured at 7σ), (i) and atomic model, (ii), of the IL-11 Δ_{10} /IL-11R α_{D1-D3} /gp130 $_{EC}$ complex. The position of the D5-D6 domains of gp130 is indicated as transparent ribbons. These domains were not included in the deposited model. Individual domains of IL-11R α and gp130 are

indicated on the cryo-EM maps. **C** X-ray electron density (contoured at 1σ , with missing F_{obs} not filled), (i), and crystal structure of the IL-11 $_{FI}$ /IL-11R α_{EC} /gp130 $_{D1-D3}$ complex, (ii), showing one hexamer of the asymmetric unit. **D** Continuous sedimentation coefficient ($c(s)$) distributions for the IL-11 Δ_{10} /IL-11R α_{D1-D3} /gp130 $_{D1-D3}$ complex and the IL-11 Δ_{10} /IL-11R α_{D1-D3} /gp130 $_{EC}$ complex. **E** SAXS data for the IL-11 Δ_{10} /IL-11R α_{D1-D3} /gp130 $_{D1-D3}$ complex and the IL-11 Δ_{10} /IL-11R α_{D1-D3} /gp130 $_{EC}$ complex.

coordinates. Together these data confirm that our atomic models represent the solution configuration of the hexameric IL-11 signalling complex.

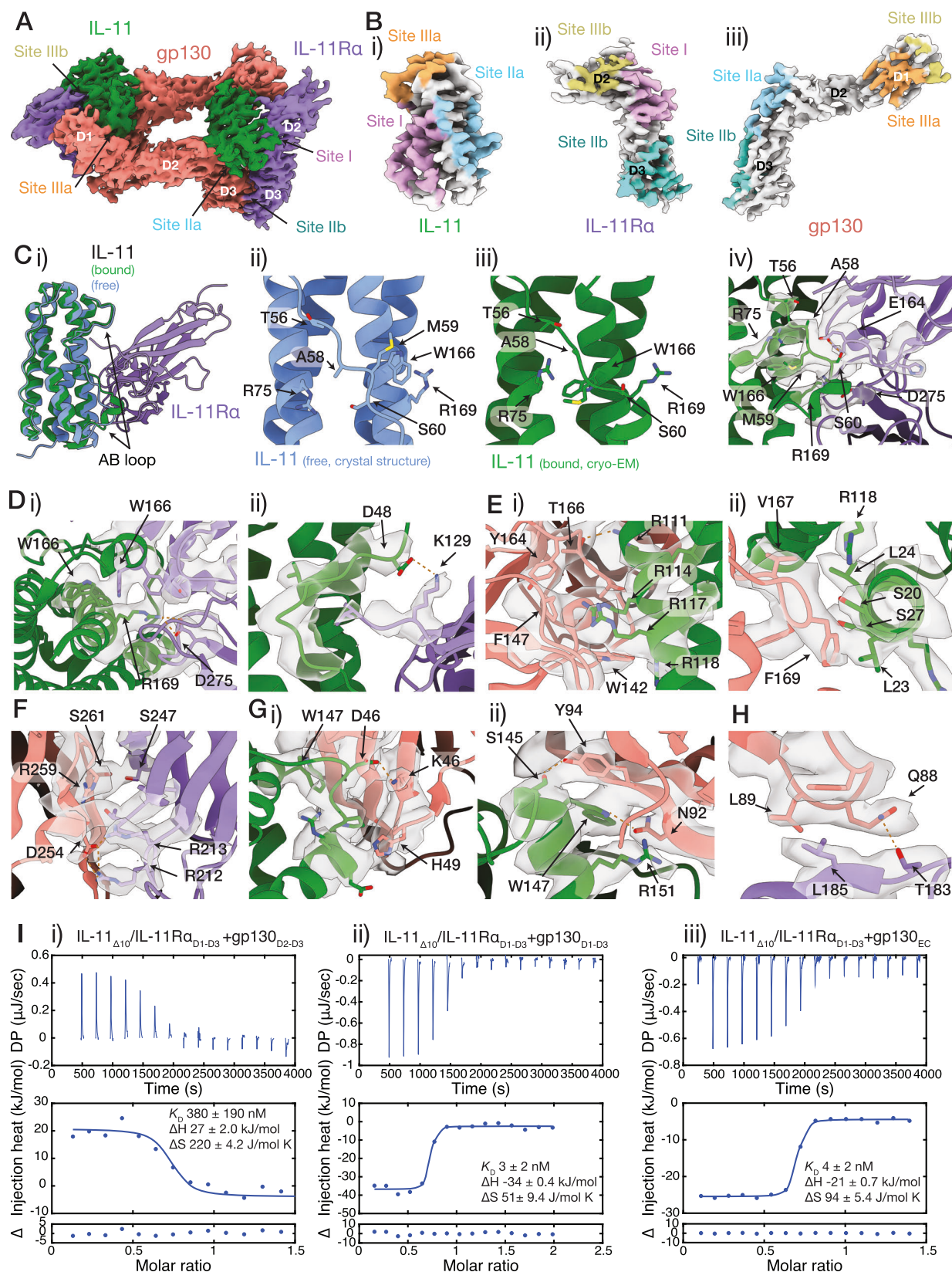
The IL-11 signalling complex forms in three steps and requires significant structural rearrangement of the cytokine

Our structures of the IL-11 signalling complex allow precise identification of the interactions forming the complex (Fig. 2A, B). Overall, complex formation results in the burying of $\sim 6450\text{ \AA}^2$ of surface area. The binding sites on IL-11 (Fig. 2B) contain residues previously identified by mutagenesis of human and mouse IL-11⁵³⁻⁵⁵ and by modelling⁴⁹. The structures reveal additional contacts between the loop joining helices A and B of the cytokine (AB loop; residues F43-G65) and IL-11R α in site-I and gp130 in site-III that have not previously been identified or interrogated (Fig. 2C, D).

Initial formation of a 1:1 complex between IL-11 and IL-11R α is mediated through site-I of the cytokine (Fig. 2C, D). The interaction has an affinity of 23 nM ⁴⁹ and is strongly driven by entropy, burying $\sim 1000\text{ \AA}^2$ of surface area. The C-terminal section of the AB loop undergoes a rearrangement upon complex formation, relative to uncomplexed IL-11⁴⁹ (Fig. 2C), resulting in significant conformational change of residues 58-68, including unfolding of the N-terminal turn of helix B. A cation- π interaction between R169 and W166 in

uncomplexed IL-11⁴⁹ is broken on complex formation, allowing the AB loop to adopt a new conformation and form extensive contacts with IL-11R α (Fig. 2Cii-iv). The rearrangement allows R169 of IL-11 to protrude into a hydrophobic pocket formed by F165, F230, and L277 of IL-11R α , and to form a potential salt bridge with D275 (Fig. 2Civ, Di). S60 and the backbone amide of M59 within the AB loop both form potential hydrogen bond networks with E164 of IL-11R α after rearrangement of the AB loop. The key roles of R169 of IL-11 in mediating both contacts with IL-11R α and conformational change of the AB loop and helix B are consistent with the significant reduction in affinity of IL-11 for IL-11R α upon substitution of R169 with alanine⁴⁹. Notably, the new position of the AB loop is stabilised by several new intra-IL-11 contacts, including a potential hydrogen bond formed by the δ -sulfur of M59 and the indole nitrogen of W166, and two potential hydrogen bonds formed by the guanidinium group of R75 with backbone atoms of T56 and A58 in the AB loop (Fig. 2Ciii). Several additional contacts are formed by the N-terminal end of the AB loop, including a potential salt bridge between D48 on the cytokine and K129 on IL-11R α (Fig. 2Dii). However, these contacts do not result in conformational change in this region of the cytokine.

After binding IL-11R α , IL-11 engages two molecules of gp130, via site-II and site-III, to form the hexameric signalling complex (Fig. 2E-H). Site-III interactions are mediated by D1 of gp130



suggesting sequential complex assembly via site-II followed by site-III. To probe the intermediate in IL-11 complex assembly, we generated gp130 $_{D2-D3}$, which lacks D1. SV-AUC of the IL-11 $_{\Delta 10}$ /IL-11Ra $_{D1-D3}$ /gp130 $_{D2-D3}$ complex (gp130 $_{D2-D3}$ complex) yields a single species with sedimentation coefficient of 4.0 S, and molecular weight of 78.2 kDa (f/f_0 : 1.6; calculated Mw: 73.5 kDa), suggesting a trimeric stoichiometry

(Supplementary Fig. 5F, G). MALS further supports a trimeric stoichiometry ($M_w = 70.6$ kDa, Supplementary Fig. 5A). SAXS data for the gp130 $_{D2-D3}$ complex fit well to a model of the trimer comprising one molecule of each component assembled via site-I and site-II (Supplementary Fig. 6B, E, Supplementary Table 3), further indicating that this trimeric complex is a stable intermediate in the complex assembly.

Fig. 2 | Interactions forming the IL-11 signalling complex. Bound IL-11 is depicted in green, IL-11R α in purple, and gp130 in salmon. **A** Structure of the IL-11 $_{\Delta 10}$ /IL-11R α_{D1-D3} /gp130 $_{D1-D3}$ complex, with the five binding sites indicated. **B** Binding surfaces on (i) IL-11, (ii) IL-11R α , and (iii) gp130. **C** Rearrangement of the AB loop on complex formation. Uncomplexed IL-11 is depicted in blue. (i) overlay of the crystal structure of IL-11 $_{\Delta 10}$ ⁴⁹ (PDB ID: 6O4O) with the structure of the complex, showing the AB loop (F43-G65) rearrangement on complex formation. (ii) interactions within the AB loop, and between the AB loop and the α -helical core in the unbound state. (iii) and (iv) the AB loop rearrangement on complex formation. **D** Details of site-I contacts (IL-11, green; IL-11R α , purple; gp130 salmon). (i) R169 of IL-11 protrudes into a pocket formed by several hydrophobic residues on IL-11R α , (ii) contacts between the N-terminal end of the AB loop of IL-11 and IL-11R α . **E** Details of

site-IIA contacts, (i) contacts between C-helix arginine residues of IL-11 and gp130, (ii) contacts between the N-terminal end of the A helix of IL-11 and gp130. **F** Details of site-IIB contacts. **G** Details of site-IIIA contacts. (i) contacts between W147 and the N-terminal end of the AB loop of IL-11 with D1 of gp130, (ii) contacts between W147 and neighbouring residues of IL-11 with D1 of gp130. **H** Details of site-IIIB contacts. Cryo-EM density maps are contoured at 7 σ . **I** Representative ITC data for (i) the interaction between the IL-11 $_{\Delta 10}$ /IL-11R α_{D1-D3} binary complex and gp130 $_{D2-D3}$; (ii) the interaction between the IL-11 $_{\Delta 10}$ /IL-11R α_{D1-D3} binary complex and gp130 $_{D1-D3}$; and (iii), the interaction between the IL-11 $_{\Delta 10}$ /IL-11R α_{D1-D3} binary complex and gp130 $_{EC}$. Representative of $n = 3$ independent experiments. For complete thermodynamic parameters, see Supplementary Table 4.

The interaction between the binary IL-11/IL-11R α complex and the first molecule of gp130 comprises two coupled interfaces: (1) between IL-11 and gp130 (site-IIA, Fig. 2E), and (2) between IL-11R α and gp130 (site-IIB, Fig. 2F). The interactions bury $\sim 700 \text{ \AA}^2$ and 600 \AA^2 respectively. The site-IIA interface is hydrophobic in character and the main contact area between IL-11 and gp130 is located on helices A and C of IL-11. Important contacts are mediated by four arginine residues of IL-11 (I11, I14, I17 and I18) and two loops of gp130 (residues 142-147 and 164-172) (Fig. 2Ei). Key contacts are formed by R114, which protrudes into an aromatic pocket formed by W142 and F147 of gp130. Residues W142 and F169 of gp130 also form important interactions. F169 interacts with the central section of helix A of IL-11, forming hydrophobic contacts with L23 and L24 (Fig. 2Eii). F196 of gp130 has been shown to also form key contacts with other IL-6 family cytokines^{56,57}. The site-IIB interaction is electrostatic in nature, and results in the formation of ten potential hydrogen bonds between D3 of IL-11R α and D3 of gp130 (Fig. 2F).

The final interaction to form the complex is a coupled interaction between IL-11 and gp130 D1 (site-IIIA) (Fig. 2G) and between IL-11R α D2 and gp130 D1 (site-IIIB) (Fig. 2H). The interaction buries $\sim 800 \text{ \AA}^2$ in surface area; $\sim 600 \text{ \AA}^2$ at site-IIIA, and 200 \AA^2 at site-IIIB. Assembly of the hexamer occurs via two symmetrical site III interfaces between the two IL-11/IL-11R α /gp130 trimers. The primary contact within site-IIIA is formed by the side chain of W147 of IL-11, which binds flat against a β -strand of gp130 D1 (Fig. 2G), with the indole nitrogen forming a potential hydrogen bond to N92 (Fig. 2Gi). Contacts are also formed by R151 and S145 of IL-11, which are adjacent to W147 (Fig. 2Gi). A second set of interactions are formed by the N-terminal end of the IL-11 AB loop, where P44 packs against D1 of gp130, and D46 forms hydrogen bonds with K46 and N82 of gp130 (Fig. 2Gii). A small interface is formed at site-IIIB between a β -sheet (residues 183-187) of IL-11R α D2 and a loop of gp130 D1 (residues 86-89) (Fig. 2H). L185 of IL-11R α forms hydrophobic contacts with L89 of gp130 and a potential hydrogen bond is formed between Q88 of gp130 and T183 of IL-11R α (Fig. 2H).

We used isothermal titration calorimetry (ITC) to study the thermodynamics of complex assembly (Fig. 2I; Supplementary Table 4). The interaction of the IL-11 $_{\Delta 10}$ /IL-11R α_{D1-D3} binary complex with gp130 $_{D2-D3}$ to form the trimer is endothermic, has moderate affinity (K_D 380 ± 190 nM, ΔH 27 ± 2 kJ/mol; Fig. 2Ii), and is strongly driven by entropy. The interaction between the IL-11 $_{\Delta 10}$ /IL-11R α_{D1-D3} complex and gp130 $_{D1-D3}$, which includes symmetrical interactions of both molecules of gp130 within the hexamer, is exothermic and relatively high affinity (K_D 3 ± 2 nM, ΔH -34 ± 0.4 kJ/mol; Fig. 2Iii).

The free energies of binding of the IL-11 $_{\Delta 10}$ /IL-11R α_{D1-D3} binary complex with gp130 $_{D2-D3}$ (ΔG -36 ± 1.7 kJ/mol) and gp130 $_{D1-D3}$ (ΔG -49 ± 3.0 kJ/mol) indicate that the ΔG associated with each gp130 D1 binding at site-III is -7 kJ/mol. Thus, the affinity of a single gp130 molecule at site-III is low (K_D -mM) and it is the avidity of the symmetrically duplicated site-III interactions that maintains hexameric complex formation. The affinity of the IL-11R α_{D1-D3} /IL-11 $_{\Delta 10}$ binary complex for gp130 $_{EC}$ (K_D 4 ± 2 nM, ΔH -20 ± 1 kJ/mol; Fig. 2Iiii) is very similar to the affinity for gp130 $_{D1-D3}$, indicating that the

membrane-proximal (D4-D6) domains of gp130 do not contribute substantially to complex formation.

Gp130 is shared by most members of the IL-6 family of cytokines. The structure of the hexameric IL-6 signalling complex³⁵ showed site-II and site-III interactions with gp130 that are similar to those of the IL-11 complex (Supplementary Fig. 7A-E), and the LIF/gp130 complex structure comprises a comparable site-II interaction³⁷ (Supplementary Fig. 7A, B). However, the molecular details of the interactions between the three cytokines differ (Supplementary Fig. 7B, C, E; see also Supplementary Discussion). Specifically, the IL-11 site-II interaction buries a larger surface area and is more electrostatic in nature, with a higher number of potential hydrogen bonds. In contrast, the IL-11 site-III interaction surface is smaller than that of IL-6 and does not involve the N-terminus of gp130.

The membrane proximal domains of gp130 are highly dynamic

The crystal structure of the extracellular domains of gp130⁵⁸ and low resolution electron microscopy studies of the IL-11⁵⁰, IL-6^{51,52}, and LIF⁵⁹ signalling complexes suggest that the membrane proximal domains, D4-D6, are responsible for correctly positioning the transmembrane and intracellular domains of the two signalling receptors. This configuration is thought to orient intracellularly bound JAK molecules for activation, and deletion of any of D4-D6 renders gp130 non-functional in vitro^{60,61}.

Our consensus maps of the gp130 $_{EC}$ complex showed well-defined density for the domains involved in complex formation (D2-D3 of IL-11R α , IL-11, and D1-D3 of gp130), and poorer density for gp130 D4-D6 (Fig. 1B; Supplementary Fig. 2Cii, Dii). We considered the possibility that structural dynamics of gp130 D4-D6 contributed to the decreasing density quality with distance from the cytokine binding regions. To explore this, we used 3D variability analysis (3DVA)⁶² in cryoSPARC⁶³, which resolves conformational changes by fitting the multiple conformations captured in the cryo-EM particle set to a continuous linear subspace model (Fig. 3, Supplementary Fig. 8A-C). 3DVA analysis of the gp130 $_{EC}$ complex cryo-EM data reveals three major variability components (Fig. 3A-C). The first has minor motion (Fig. 3A; Supplementary Movie 1), the second corresponds to a side-to-side oscillation of D4-D6 of gp130 (Fig. 3B; Supplementary Movie 2), and the third corresponds to an inward swinging motion of D4-D6 relative to the rest of the complex (Fig. 3C, Supplementary Movie 3). Histograms of the distributions along each trajectory are unimodal, indicating continuous motion (Fig. 3D, Supplementary Fig. 8A-C). This analysis shows that the D4-D6 region of gp130 is dynamic and is not stabilised upon complex formation. A multistate model, allowing flexibility of gp130 domains D4-D6 and IL-11R α D1, fit the SAXS data for the gp130 $_{EC}$ complex better than our single consensus model of the complex (Supplementary Fig. 8D, E; Supplementary Table 3), further supporting flexibility of these domains within the complex. The proposed flexibility of D4-D6 of gp130 is also in agreement with our ITC results, showing that the gp130 $_{EC}$ complex forms with similar affinity to the gp130 $_{D1-D3}$ complex, and is supported by our previous molecular dynamics (MD) simulations of gp130 D2-D5 showing that D4 is dynamic with respect to D3⁶⁴.

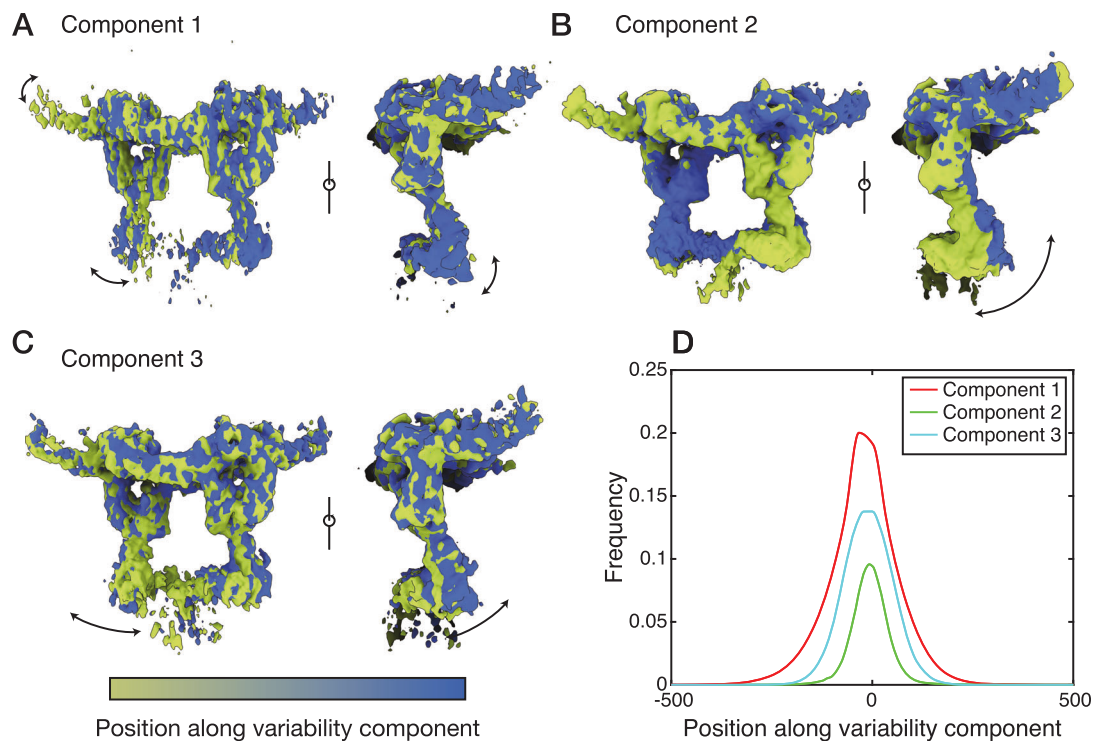


Fig. 3 | 3D variability analysis of the gp130_{EC} complex cryo-EM map. Refined consensus densities along, (A) variability component 1, (B) variability component 2, (C) variability component 3. Density maps are coloured according to the relative

position along the variability component and arrows indicate approximate motions of the receptor domains. **D** Frequency distributions of the number of particles contributing to each variability component (see also Supplementary Fig. 8).

Together these data indicate that D4-D6 of gp130 do not contribute to complex formation. Despite the separation of the C-termini of D6 in the consensus model (Supplementary Fig. 8F), the 5–6 residue linker between D6 and the transmembrane helix segment may allow interaction of the two gp130 transmembrane helices of the complex in a parallel configuration.

The cytokine variant, IL-11 Mutein, potently inhibits IL-11 signalling in human cells

IL-11 mutants have previously been proposed to competitively inhibit IL-11 signalling^{43,44}. The IL-11 W147A mutation⁴⁴ removes the key tryptophan residue in site-III responsible for the final step of hexameric complex formation (Fig. 2Gi). Phage display was subsequently used to identify variants with higher inhibitory potency resulting in IL-11 Mutein, which contains W147A combined with mutations of AB loop residues 58–62, ⁵⁸AMSAG⁶² to ⁵⁸PAIDY⁶², that were reported to increase affinity to IL-11R α ⁴³.

To characterise these mutants, we generated recombinant human IL-11 Δ ₁₀/W147A, IL-11 Δ ₁₀/Mutein, and a variant containing only the ⁵⁸PAIDY⁶² mutations, which we termed IL-11 Δ ₁₀/PAIDY. We assessed the biological activity of IL-11 Δ ₁₀/W147A, IL-11 Δ ₁₀/Mutein and IL-11 Δ ₁₀/PAIDY in Ba/F3 cells stably expressing human gp130 and IL-11R α ⁶⁵ by measuring STAT3 activation, indicated by phosphorylation at Y705 (pSTAT3), using flow cytometry (Fig. 4; Supplementary Fig. 9). As expected, stimulation with IL-11 Δ ₁₀ produces a robust pSTAT3 response, with an EC₅₀ of 12 ± 1.1 pM (Fig. 4A; Supplementary Fig. 9A). Conversely, stimulation with IL-11 Δ ₁₀/Mutein alone does not result in STAT3 activation (Fig. 4A; Supplementary Fig. 9A), demonstrating that the mutations eliminate the ability of IL-11 Δ ₁₀/Mutein to signal, in agreement with previous reports⁴³. Surprisingly, stimulation with either IL-11 Δ ₁₀/W147A or IL-11 Δ ₁₀/PAIDY resulted in robust STAT3 activation, albeit with a higher EC₅₀ than IL-11 Δ ₁₀, of 610 ± 120 pM ($p = 0.04$ vs IL-11 Δ ₁₀) and 140 ± 12 pM ($p = 0.01$ vs IL-11 Δ ₁₀), respectively.

We also examined the inhibitory activity of IL-11 Δ ₁₀/Mutein, IL-11 Δ ₁₀/W147A and IL-11 Δ ₁₀/PAIDY in Ba/F3 cells (Fig. 4B; Supplementary Fig. 9B).

IL-11 Δ ₁₀/Mutein strongly inhibited IL-11 Δ ₁₀ mediated STAT3 activation (IC₅₀ = 850 ± 275 nM, Fig. 4B), validating IL-11 Δ ₁₀/Mutein as an effective inhibitor of IL-11 signalling. In contrast, neither IL-11 Δ ₁₀/W147A or IL-11 Δ ₁₀/PAIDY inhibited IL-11 Δ ₁₀ mediated STAT3 activation, contradicting previous reports that the W147A mutation alone is an effective IL-11 signalling inhibitor^{44,66,67}. Overall, these results show that the inhibitory effect of IL-11 Δ ₁₀/Mutein requires the combination of both the W147A and ⁵⁸PAIDY⁶² mutations, with either variant alone insufficient to inhibit STAT3 phosphorylation via IL-11 signalling.

We extended these studies to several human cell lines and showed that IL-11 Δ ₁₀ robustly stimulates STAT3 activation in the breast cancer cell line MDA-MD-231, the lung cancer cell line A549, the glioblastoma cell line U87-MG, the pancreatic cancer cell line BxPC3, and the prostate cancer cell line LnCap (Fig. 4C), in keeping with the tumorigenic function of IL-11. In each of these human cell lines, IL-11 Δ ₁₀/Mutein effectively inhibits IL-11 mediated STAT3 activation.

IL-11 Mutein blocks the final step of hexamer assembly

Our functional results prompted investigation of the structural mechanism of IL-11 Mutein signalling inhibition. SV-AUC of the IL-11 Δ ₁₀/Mutein/IL-11R α _{D1-D3}/gp130_{D1-D3} complex yielded a single peak in the sedimentation coefficient distribution of 4.5S and estimated mass 88.9 kDa (f/f_0 : 1.6), consistent with the formation of a homogenous trimeric complex (Fig. 5Ai; Supplementary Fig. 10Ai).

SV-AUC of the IL-11 Δ ₁₀/W147A/IL-11R α _{D1-D3}/gp130_{D1-D3} complex indicates that the W147A mutant predominantly forms a trimeric complex (sedimentation coefficient: 4.5S, mass: 82.7 kDa, f/f_0 : 1.5; Fig. 5Aii; Supplementary Fig. 10Aii). However, a small population of hexameric complex at -7.5S was observed in the sedimentation coefficient distributions, indicating that the W147A mutation alone permits some hexamer formation and consistent with the ability of IL-11 Δ ₁₀/W147A to stimulate STAT3 activation in vitro (Fig. 4A). SV-AUC of the IL-11 Δ ₁₀/PAIDY/IL-11R α _{D1-D3}/gp130_{D1-D3} yields a single species with sedimentation coefficient of 6.8S, and mass of 184.3 kDa (f/f_0 : 1.7),

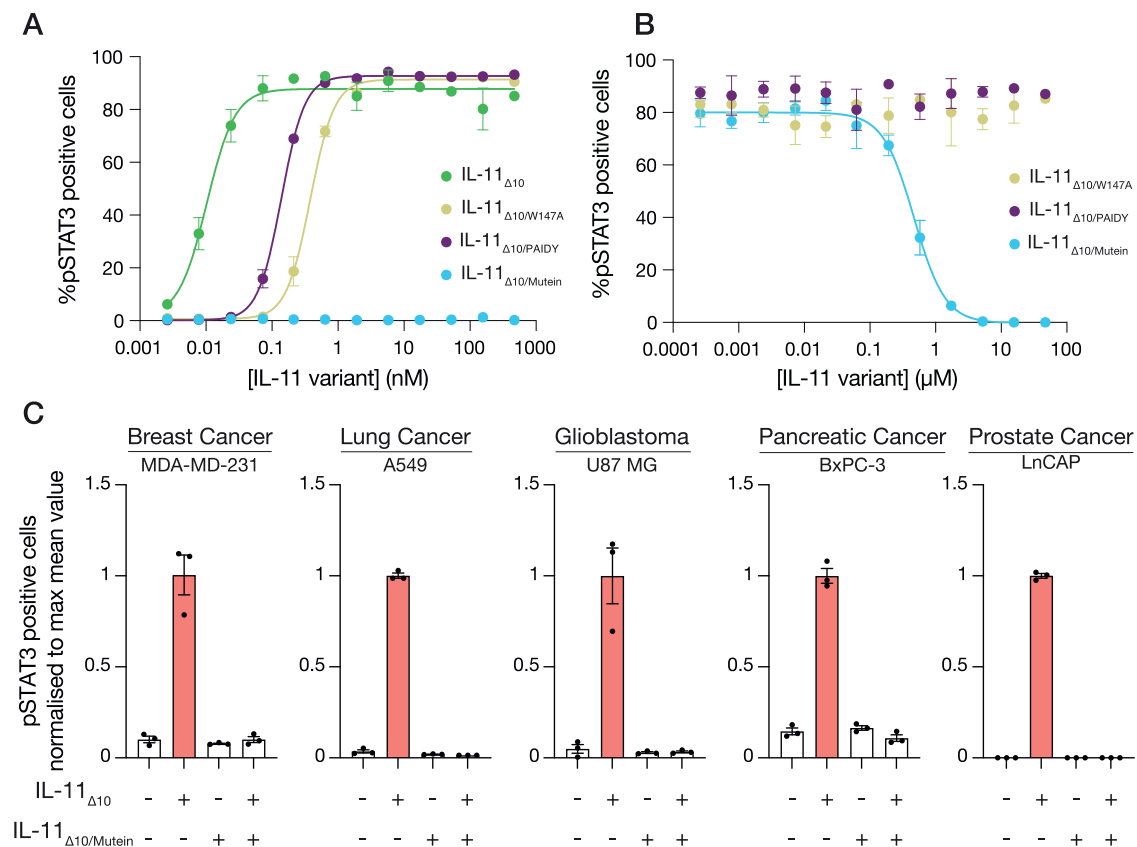


Fig. 4 | IL-11 Mutein is an effective inhibitor of human IL-11 signalling in vitro.

A Representative dose-response curve for IL-11 or IL-11 variant stimulation. The EC_{50} for IL-11 $_{\Delta 10}$ was 0.010 ± 0.002 nM; the EC_{50} for IL-11 $_{\Delta 10/W147A}$ was 0.6 ± 0.2 nM, the EC_{50} for IL-11 $_{\Delta 10/PAIDY}$ was 0.14 ± 0.02 nM; the EC_{50} for IL-11 $_{\Delta 10/Mutein}$ could not be determined. Data are presented as the mean \pm SEM of three technical replicates. Representative of $n = 3$ independent experiments. Replicate experiments are presented in Supplementary Fig. 9A. **B** Representative dose-response curve for the inhibition of IL-11 $_{\Delta 10}$ stimulation by the IL-11 variants IL-11 $_{\Delta 10/W147A}$, IL-11 $_{\Delta 10/PAIDY}$, and

IL-11 $_{\Delta 10/Mutein}$. The IC_{50} for IL-11 $_{\Delta 10/Mutein}$ inhibition was 850 ± 275 nM, the IC_{50} for the remaining variants was not determined. Data are presented as the mean \pm SEM of three technical replicates. Representative of $n = 3$ independent experiments. Replicate experiments are presented in Supplementary Fig. 9B. **C** Potent inhibition of IL-11 $_{\Delta 10}$ signalling by IL-11 $_{\Delta 10/Mutein}$ in the indicated human cancer cell lines. Data are presented as the mean \pm SEM of three technical replicates. Representative of $n = 2$ independent experiments. Replicate experiments are presented in Supplementary Fig. 9C. Source data are provided as a Source Data file.

Fig. 5Aiii, Supplementary Fig. 10Aiii, indicating that IL-11 $_{\Delta 10/PAIDY}$ mediates formation of the hexameric complex to a similar extent to WT IL-11 $_{\Delta 10}$.

Further supporting the trimeric nature of the IL-11 $_{\Delta 10/Mutein}$ complex, SAXS data collected on the IL-11 $_{\Delta 10/Mutein}/gp130_{D1-D3}/IL-11R\alpha_{D1-D3}$ complex (Fig. 5B, Supplementary Fig. 10B) agrees well with the calculated scattering profile of a single trimer of the gp130 $_{D1-D3}$ complex. Furthermore, ab initio models from SAXS data collected on the IL-11 $_{\Delta 10/Mutein}/IL-11R\alpha_{D1-D3}/gp130_{D1-D3}$ complex and the gp130 $_{D1-D3}$ complex hexamer are consistent with the IL-11 $_{\Delta 10/Mutein}$ complex being half the size in one dimension compared to the hexameric complex (Supplementary Fig. 10C). The mass of the IL-11 $_{\Delta 10/Mutein}$ complex determined by SV-AUC and SAXS is also supported by the mass determined using MALS (M_w , 79.6 kDa, Supplementary Fig. 10D).

In combination, these results indicate that both IL-11 $_{\Delta 10/W147A}$ and IL-11 $_{\Delta 10/PAIDY}$ can mediate assembly of the hexameric signalling complex, albeit to differing extents, while formation of site III interactions by IL-11 $_{\Delta 10/Mutein}$ is abrogated, and assembly is stalled at the trimer stage.

IL-11 Mutein/IL-11R α binding kinetics are different to WT IL-11

The $^{58}PAIDY^{62}$ mutations present in the AB loop of IL-11 were proposed to increase the affinity for IL-11R α twenty-fold over WT IL-11, resulting in effective competition for IL-11R α binding⁴³. To test this, we measured the affinity of the mutant cytokines for IL-11R α using ITC (Fig. 5C). IL-11 $_{\Delta 10/W147A}$, IL-11 $_{\Delta 10/Mutein}$, and IL-11 $_{\Delta 10/PAIDY}$ interact with

IL-11R α_{D1-D3} with K_D of 10 ± 8 nM, 38 ± 9 nM, ($p = 0.2$ vs IL-11 $_{\Delta 10/W147A}$), and 81 ± 44 nM, ($p = 0.3$ vs IL-11 $_{\Delta 10/W147A}$) respectively (Fig. 5C). These data suggest that the PAIDY mutations do not significantly increase the affinity of IL-11 for the IL-11R α .

We also measured binding kinetic parameters for IL-11 $_{\Delta 10}$ and IL-11 $_{\Delta 10/Mutein}$ with IL-11R α_{D1-D3} using surface plasmon resonance (SPR). IL-11 constructs were C-terminally biotinylated via an avitag⁶⁸ and coupled to a streptavidin SPR chip (Fig. 5D). Despite similar affinity, the kinetics of the interactions were different, with approximately three-fold slower dissociation rate for IL-11 $_{\Delta 10/Mutein}/IL-11R\alpha_{D1-D3}$ (k_d $0.34 \pm 0.01 \times 10^{-1} s^{-1}$, Fig. 5Di) than IL-11 $_{\Delta 10}/IL-11R\alpha_{D1-D3}$ (k_d $1.1 \pm 0.2 \times 10^{-1} s^{-1}$; Fig. 5Dii $n = 2$; Supplementary Table 5; $p = 0.06$ vs IL-11 $_{\Delta 10/Mutein}$).

These results show that the PAIDY mutations present in IL-11 $_{\Delta 10/Mutein}$ alter the kinetics of interaction with IL-11R α , compared to IL-11, but do not significantly alter the affinity (Fig. 5C, $p = 0.2$ IL-11 $_{\Delta 10/Mutein}$ vs IL-11 $_{\Delta 10/W147A}$), suggesting that the mechanism of signalling inhibition by IL-11 Mutein is more complex than previously appreciated.

The conformation of the AB loop of IL-11 Mutein is altered relative to WT IL-11

We solved crystal structures of IL-11 $_{\Delta 10/Mutein}$ and IL-11 $_{\Delta 10/W147A}$ at resolutions of 1.8 Å and 1.5 Å, respectively, to understand the structural consequences of the mutations (Fig. 6A, B; Supplementary Fig. 11A–D; Supplementary Table 2). SAXS experiments show that the crystal structures are representative of the solution structure, and SV-AUC

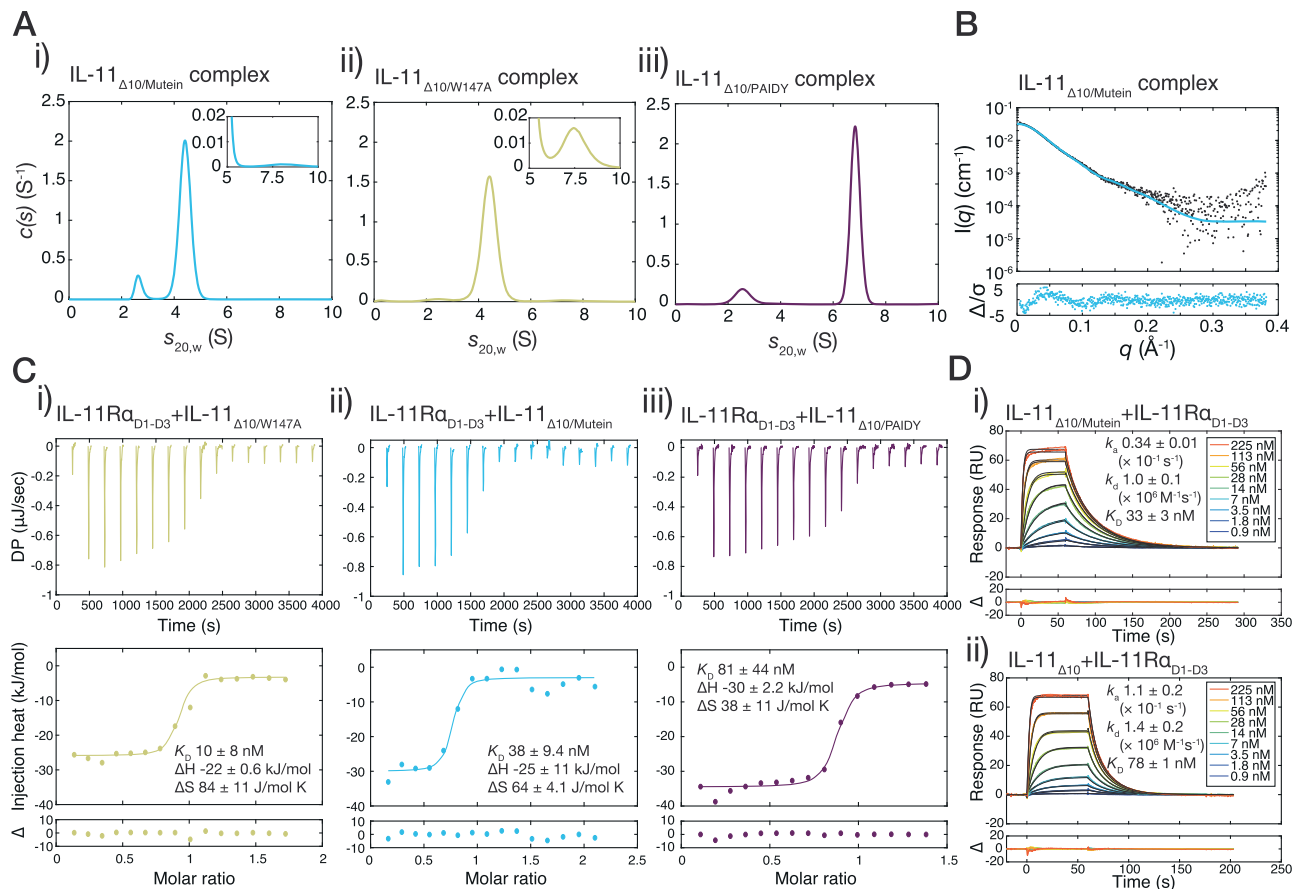


Fig. 5 | Biophysical basis for IL-11 Mutein signalling inhibition. **A** Continuous sedimentation coefficient ($c(s)$) distributions for the complexes formed between IL-11Rα_{D1-D3}, gp130_{D1-D3} and (i) IL-11_{Δ10/Mutein}, (ii) IL-11_{Δ10/W147A}, (iii) IL-11_{Δ10/PAIDY}. Insets show expanded detail of the 5–10 S region. **B** SAXS data for the IL-11Rα_{D1-D3}/gp130_{D1-D3}/IL-11_{Δ10} Mutein complex. The fit shown is to a model of the trimeric complex, χ^2 1.7 (see Methods). **C** Representative ITC data for the interaction between IL-11Rα_{D1-D3} and (i) IL-11_{Δ10/W147A}, (ii) IL-11_{Δ10/Mutein}, and (iii) IL-11_{Δ10/PAIDY}.

Representative of $n = 3$ independent experiments. **D** SPR data for the interaction between IL-11Rα_{D1-D3} and (i) biotinylated IL-11_{Δ10/Mutein} and (ii) biotinylated IL-11_{Δ10}. Black lines show the fit to the data. Representative of $n = 2$ independent experiments. In both experiments, the biotin tag was used to immobilise IL-11_{Δ10} or IL-11_{Δ10} Mutein to a streptavidin sensor chip. For complete thermodynamic and kinetic parameters for the ITC and SPR experiments, see Supplementary Tables 4 and 5, respectively.

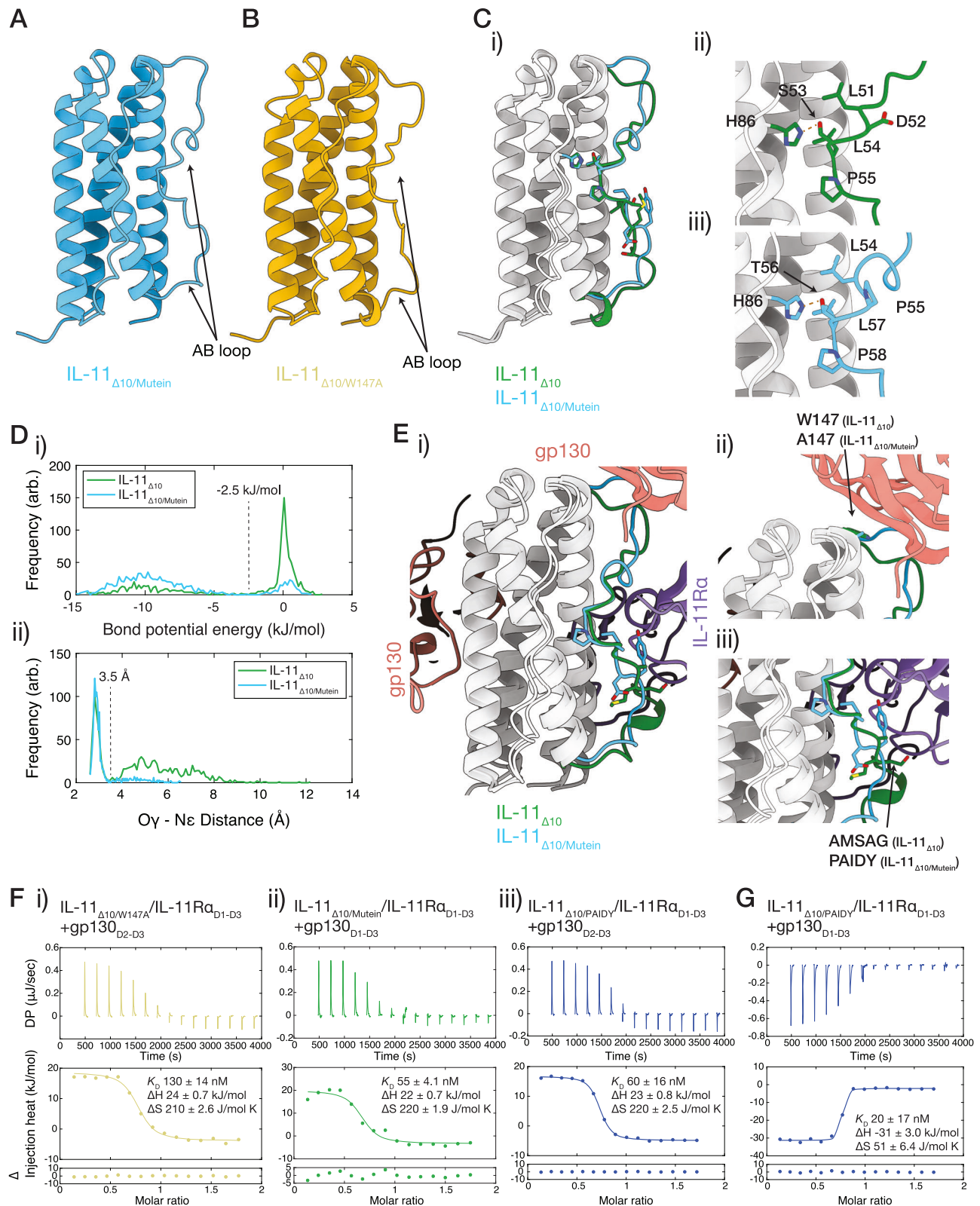
indicates that both proteins are monomeric in solution (Supplementary Fig. 11E, F; Supplementary Fig. 12).

The structure of IL-11_{Δ10/W147A} is similar to the structure of IL-11_{Δ10} (Supplementary Fig. 11G; RMSD 0.3 Å relative to IL-11_{Δ10}⁴⁹), indicating that the W147A mutation does not alter the structure. In contrast, the AB loop of IL-11_{Δ10/Mutein} shows significant conformational shifts relative to the WT structure caused by alterations in key contacts between the loop and the four- α -helical bundle (Fig. 6Ci; Supplementary Fig. 11Gii; RMSD 1.3 Å relative to IL-11_{Δ10}⁴⁹). The nature of the crystal contacts formed by the AB loop is similar in each crystal structure, comprising primarily contacts with the AB loop and CD loop of neighbouring molecules (Supplementary Fig. 11C, D), with the bulk of the loop surrounded by solvent. This suggests that the crystal packing does not constrain the configuration of the AB loop.

In IL-11_{Δ10}⁴⁹ and IL-11_{Δ10/W147A}, a hydrogen bond is formed between the side chains of S53 within the AB loop and H86 on helix B (Fig. 6Cii). In contrast, in IL-11_{Δ10/Mutein} this hydrogen bond is formed between T56 of the loop and H86 (Fig. 6Ciii; for overlay see Supplementary Fig. 11H). Furthermore, key hydrophobic interactions between AB loop residues L51, L54 and P55 and the helical bundle of IL-11_{Δ10} and IL-11_{Δ10/W147A} (Fig. 6Cii; Supplementary Fig. 11I) are mediated by L54, L57 and P58 in IL-11_{Δ10/Mutein} (Fig. 6Ciii; Supplementary Fig. 11Ii). Thus, the S⁸PAIDY⁶² mutations alter the position of the AB-loop, shifting the register of key loop-core interactions by three residues, while maintaining the composition of the interacting residues. This register change is due to a

shift of the LX(S/T)LP motif that mediates loop-core contacts: In IL-11_{Δ10} and IL-11_{Δ10/W147A} the motif is ⁵¹LDSL⁵⁵, while in IL-11_{Δ10/Mutein} the interacting motif is ⁵⁴LPTL⁵⁸. The result is that the bulk of the loop is shifted toward site-III and the N-terminal turn of helix-B is unfolded. We note that this configuration of the C-terminal segment of the AB-loop and N-terminal turn of helix-B resembles the structure of wild-type IL-11_{Δ10} bound within the hexameric complex.

To assess the dynamics of the AB loop, we performed 1 μ s molecular dynamics simulations of both IL-11_{Δ10} and IL-11_{Δ10/Mutein} (Fig. 6D; Supplementary Fig. 13; Supplementary Movies 4, 5). The overall dynamic profile of the four- α -helical core of the two proteins is very similar (Supplementary Fig. 13A–C). We analysed the stability of the IL-11_{Δ10} S53-H86 hydrogen bond and the IL-11_{Δ10/Mutein} T56-H86 hydrogen bond throughout the simulation by calculating the distance between the donor (S53 O γ or T56 O γ) and the acceptor (H86 N ϵ), and the distribution of the potential hydrogen bond energy (Fig. 6D; Supplementary Fig. 13D–F). Using a hydrogen bond energy cut-off of -2.5 kJ/mol, S53 of IL-11_{Δ10} is hydrogen bonded to H86 for 33% of the simulation, while T56 of IL-11_{Δ10/Mutein} is hydrogen bonded to H86 for 84% of the trajectory. This increased persistence of the hydrogen bond suggests that the AB loop conformation of IL-11_{Δ10/Mutein} is more stable than that of IL-11_{Δ10}. Differential scanning fluorometry (DSF) analysis revealed that the temperature of hydrophobic exposure (T_h^{69}) of IL-11_{Δ10/Mutein} was 88.7 ± 0.16 °C indicating significantly higher thermal stability than



both IL-11_{Δ10} (T_h 84.8 ± 0.39 °C, p = 0.003 vs IL-11_{Δ10/Mutein}) and IL-11_{Δ10/W147A} (T_h 87.3 ± 0.29 °C, p = 0.04 vs IL-11_{Δ10/Mutein}) (Supplementary Fig. 14A).

Together these data indicate that altered loop-core interactions brought about by the ⁵⁸PAIDY⁶² mutations in IL-11_{Δ10/Mutein} result in a new, stabilised position of the AB loop. We propose that this improved stability is due to the backbone structural restraints introduced in the IL-11_{Δ10/Mutein} LX(S/T)LP motif by P55 at the X position.

The AB loop of IL-11 Mutein acts in combination with the W147A mutation to block hexamer formation at site-III

Our IL-11 complex structures show that the N-terminal section of the AB loop contacts gp130 at site-III, suggesting that the altered conformation and stability of the AB loop in IL-11_{Δ10/Mutein} could alter interactions at this site. Superposition of the crystal structure of IL-11_{Δ10/Mutein} with an IL-11 molecule of our gp130_{D1-D3} complex structure (Fig. 6E) revealed that the N-terminal part of the AB-loop of

Fig. 6 | The structure of IL-11 Mutein, and mechanism of inhibition. A The structure of IL-11 Δ_{10} Mutein. **B** The structure of IL-11 Δ_{10} /W147A. **C** Overlay of IL-11 Δ_{10} Mutein and IL-11 Δ_{10} (PDB ID: 6O4O⁴⁵); (i) overall view of both structures, with the AB loop coloured as indicated in the figure. (ii) detail of the AB loop, showing changes in loop-core interaction that occur as a result of the PAIDY mutations in IL-11 Mutein. **D** MD analysis of the hydrogen bond between S53/T56 and H86. (i) distribution of the estimated bond potential energy for IL-11 Δ_{10} and IL-11 Δ_{10} Mutein through the simulation, an approximate cut-off for hydrogen bonding is indicated. (ii) distance distribution for the distance between the donor oxygen (S53/T56 Oy) and the acceptor nitrogen (H86 Ne) through the simulation, an approximate cut-off for hydrogen bonding is indicated. **E** Overlay of the structure of IL-11 Δ_{10} Mutein with

the structure of the IL-11R α_{D1-D3} /gp130 $_{D1-D3}$ /IL-11 Δ_{10} complex. (i) overall view. (ii) detail of the site-III interface, with the W147/A147 residue shown. (iii) detail of the AB loop, with the AMSAG/PAIDY residues shown. **F** Representative ITC data for (i) the interaction between the IL-11 Δ_{10} /W147A/IL-11R α_{D1-D3} binary complex and gp130 $_{D2-D3}$; (ii) the interaction between the IL-11 Δ_{10} /Mutein/IL-11R α_{D1-D3} binary complex and gp130 $_{D1-D3}$; and (iii) the interaction between the IL-11 Δ_{10} /PAIDY/IL-11R α_{D1-D3} binary complex and gp130 $_{D2-D3}$ complex. Representative of $n = 3$ independent experiments. **G** Representative ITC data for the interaction between the IL-11 Δ_{10} /PAIDY/IL-11R α_{D1-D3} binary complex and gp130 $_{D1-D3}$. Representative of $n = 3$ independent experiments. For complete thermodynamic parameters, see Supplementary Table 4.

IL-11 Δ_{10} /Mutein clashes sterically with D1 of gp130 at site-III in the complex (Fig. 6Eii). This observation suggested that the altered conformation of the AB-loop acts to disrupt gp130 binding at site-III.

To investigate this possibility, we determined the affinities of the IL-11 Δ_{10} /W147A/IL-11R α_{D1-D3} , IL-11 Δ_{10} /PAIDY/IL-11R α_{D1-D3} , and IL-11 Δ_{10} /Mutein/IL-11R α_{D1-D3} binary complexes for gp130 (Fig. 6F–G; Supplementary Table 4). The IL-11 Δ_{10} /W147A/IL-11R α_{D1-D3} binary complex binds gp130 $_{D2-D3}$, forming a trimeric complex, with similar affinity to IL-11 Δ_{10} (K_D 130 \pm 14 nM, $p = 0.15$ vs IL-11 Δ_{10} ; Fig. 6Fi). In contrast, the interaction of IL-11 Δ_{10} /Mutein/IL-11R α_{D1-D3} with gp130 $_{D1-D3}$ and IL-11 Δ_{10} /PAIDY/IL-11R α_{D1-D3} with gp130 $_{D2-D3}$ to form a trimer was significantly higher affinity than WT IL-11 Δ_{10} , with K_D of 55 \pm 4 nM, ($p = 0.01$ vs IL-11 Δ_{10}) (Fig. 6Fii) and 60 \pm 16 nM ($p = 0.04$ vs IL-11 Δ_{10}) (Fig. 6Fiii), respectively. Interestingly, IL-11 Δ_{10} /PAIDY/IL-11R α_{D1-D3} binds gp130 $_{D1-D3}$ to form the hexameric complex with similar affinity compared to IL-11 Δ_{10} (K_D 20 \pm 17 nM, $p = 0.2$ vs IL-11 Δ_{10} ; Fig. 6G; Supplementary Table 4).

These ITC results show that the PAIDY mutations increase site-II affinity but are insufficient to disrupt hexamer formation in the absence of the W147A mutation. These observations are consistent with our biological assays (Fig. 4), indicating that the synergistic effects of the PAIDY and W147A mutations are required for the potent antagonist function of IL-11 Mutein.

The increase in site-II affinity of IL-11 Δ_{10} /Mutein and IL-11 Δ_{10} /PAIDY was surprising, given that the mutations in both proteins lie distant from the site-II interface (Fig. 6E). This increased affinity may be explained by the slower dissociation rate of the IL-11 Δ_{10} /Mutein/IL-11R α_{D1-D3} complex relative to the IL-11 Δ_{10} /IL-11R α_{D1-D3} complex. In this case, the increased residence time of IL-11 Δ_{10} /Mutein bound to IL-11R α_{D1-D3} increases the period that the composite site-II binding interface for gp130 is intact and, therefore, increases the frequency of productive binding collisions by gp130. Thus, the microscopic association rate of gp130 is increased with little effect on its dissociation rate. Alternatively, the altered site-II interaction may reflect modified dynamics of the bound cytokine variant or subtle adjustment of its binding pose on IL-11R α induced by the ⁵⁸PAIDY⁶² mutations.

Our ITC and SPR results, in combination with the structures of the IL-11 signalling complex, IL-11 Δ_{10} /Mutein, and IL-11 Δ_{10} /W147A show that the ⁵⁸PAIDY⁶² mutations in IL-11 Mutein significantly alter the interaction of the cytokine with both IL-11R α and gp130 at all three binding sites, which likely underpins the efficacy of IL-11 Mutein as an IL-11 signalling inhibitor. The slower dissociation rate at site I and increased affinity at site II enhance the ability of IL-11 Δ_{10} /Mutein to compete with native IL-11 for binding to IL-11R α and gp130, thereby contributing to the competitive inhibition mechanism. These results also show that the AB loop in IL-11 is a critical region for the formation of the signalling complex, which will guide future design of inhibitors.

Discussion

IL-11 signalling has been implicated in a number of human diseases and is pre-clinically validated as a therapeutic target, prompting significant investment in therapeutic development, with the first clinical trials imminent. However, informed development of IL-11 signalling inhibitors has been hindered by a lack of structural knowledge of the IL-11

complex, and a lack of understanding of the mechanism of action of existing IL-11 signalling inhibitors. We report the structures of the IL-11 signalling complex, including information on the position and dynamics of the extracellular domains of gp130, which have previously eluded high-resolution structural characterisation. We show that the complex forms in three steps (Fig. 7) involving significant conformational rearrangement of the cytokine that is coordinated by a key arginine residue, R169. These conformational changes of IL-11 upon complex formation are significantly larger than those observed for other IL-6 family members, IL-6 and LIF, and the nature of the interactions forming the IL-11 complex is distinct^{35,37,70}.

The formation of the signalling complex results in activation of JAKs bound to the cytoplasmic region of gp130, mainly JAK1 and to a lesser extent JAK2 and TYK2. Activated JAKs subsequently phosphorylate tyrosine residues of gp130 resulting in activation of signalling pathways, including STAT, ERK, MAPK and phosphoinositide 3-kinase (PI3K) pathways that mediate biological outcomes^{28,29}. Our data on the nature and dynamics of the membrane-proximal domains of gp130 have important implications for understanding the molecular mechanisms of JAK activation and propagation of downstream signalling pathways. The observation that D4–D6 of gp130 are flexible with respect to the membrane distal domains (D1–D3) provides information on the potential relative positions of the two D6 domains within the complex that may affect positioning of the transmembrane and cytoplasmic domains. This has implications for the relative positioning and activation of the bound JAK molecules and will inform further interrogation of signalling complexes including transmembrane and cytoplasmic machinery. In future, this knowledge may also inform how the different downstream signalling pathways are co-activated, or individually activated in disease, as evidence emerges that there may be a cell context dependent IL-11 mediated activation of STAT3 pro-survival pathways compared to IL-11 mediated ERK driven proliferation and apoptosis in disease⁷¹. Importantly, by defining the structural and biophysical dynamics of gp130 within the signalling complex our data enable a better understanding of the pathogenicity of emerging cytokine selective variants in IL6ST^{64,72–77}, as well as variants in IL11R^{78,79} and IL11^{80,81}, for which there are no targeted therapeutic opportunities for patients.

Our characterisation of the IL-11 signalling inhibitor, IL-11 Mutein, shows that it is highly effective at blocking signalling complex formation and potentially inhibits signalling in a range of human cancer cell lines, highlighting the breadth of disease applications for emerging IL-11 signalling therapeutics. In contrast, the point mutant, IL-11 W147A, does not antagonise signalling by wild-type IL-11, contradicting previous reports^{44,66,67}. In particular, our data show the importance of the IL-11 Mutein AB loop in modulating interactions with IL-11R α and both gp130 molecules of the complex leading to inhibition of signalling (Fig. 7). Thus, engineering of the AB loop may be a general path for generation of antagonist variants of class I cytokines. Our results functionally and mechanistically validate IL-11 Mutein as a tool IL-11 signalling inhibitor and provide a straightforward, high-yield method for producing IL-11 Mutein suitable for laboratory studies of IL-11 biology.

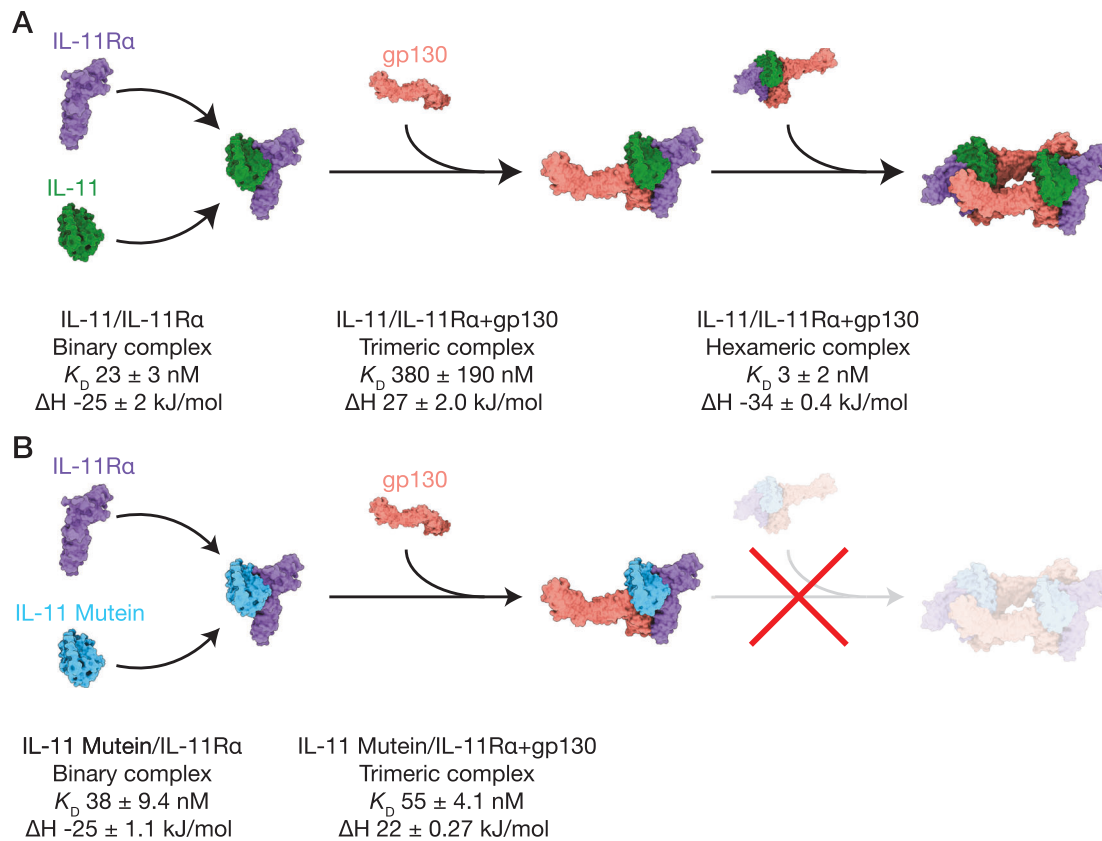


Fig. 7 | Schematic of IL-11 complex assembly, and mechanism of action of IL-11 Mutein. A Stoichiometry and thermodynamics of the three-step cooperative assembly of the IL-11 signalling complex. IL-11 and IL-11Rα form a binary complex that subsequently binds the first molecule of gp130 to form a trimeric intermediate. Two trimers then associate, resulting in a hexameric complex comprising two copies each of IL-11, IL-11Rα, and gp130. **B** The mechanism of IL-11 Mutein inhibition.

IL-11 Mutein binds IL-11Rα and the first molecule of gp130 to form a trimeric complex. However, the IL-11 Mutein/IL-11Rα/gp130 trimer cannot dimerise to form a hexameric complex and, consequently, signalling is abolished. IL-11 Mutein competitively inhibits IL-11 signalling through a reduced rate of dissociation from IL-11Rα and increased affinity for the first molecule of gp130, relative to IL-11. Complexes and subunits are displayed as solvent-accessible molecular surfaces.

Overall, the results presented here will facilitate significant advancement of IL-11 biology and will appreciably aid the development of therapeutic agents targeting IL-11 signalling and signalling by related cytokines.

Methods

Protein expression and purification

Throughout this work, we used an N-terminally truncated form of IL-11 (IL-11 Δ_{10}), and a C-terminally truncated form of IL-11Rα (IL-11Rα $_{D1-D3}$), containing the structured extracellular domains characterised previously⁴⁹. We used gp130 constructs containing the D1-D3 domains of gp130 (gp130 $_{D1-D3}$), D2-D3 domains (gp130 $_{D2-D3}$), or D1-D6 domains of gp130, which comprise the complete extracellular region of gp130 (gp130 $_{EC}$)⁵⁸.

Human IL-11, IL-11 mutants, and IL-11Rα constructs were expressed and purified as previously described⁴⁹. Human gp130 constructs were expressed using the same insect cell expression method as IL-11Rα⁴⁹. Human IL-11 and IL-11 mutants, N-terminally fused to a His₆ tag, maltose binding protein and a TEV protease cleavage site were expressed in BL21(DE3) *Escherichia coli* cells, and purified using sequential nickel-affinity, cation exchange and gel filtration chromatography. Cleavable tags were removed using TEV protease. IL-11Rα constructs and gp130 constructs, N-terminally fused to a honeybee-melittin signal peptide, His₈ tag, and TEV cleavage site were expressed in *Spodoptera frugiperda* Sf21 (Invitrogen cat. 11497013) cells using baculovirus. Proteins were purified from the conditioned media using nickel-affinity chromatography, followed by tag removal using TEV protease and gel filtration chromatography.

For coupling to a streptavidin SPR chip, we generated IL-11 Δ_{10} and IL-11 Δ_{10} /Mutein constructs with a C-terminal avitag⁶⁸, which was biotinylated in vitro in *Escherichia coli* BL21(DE3) cells. These fusion proteins were purified using identical methods to IL-11 Δ_{10} , and the degree of biotinylation was assessed using mass spectrometry.

Purification of the IL-11 signalling complex

The IL-11 signalling complex was prepared by mixing equimolar amounts of IL-11 Δ_{10} , IL-11Rα $_{D1-D3}$ and gp130 $_{D1-D3}$ /gp130 $_{EC}$. The complex was incubated on ice for -1 h, then applied to a Superdex 200 10/30 size exclusion column (Cytiva cat. 28990944), pre-equilibrated in TBS pH 8.0. Fractions containing the signalling complex were pooled and concentrated to 1.5 mg/mL. Purity of the complex was assessed using native-PAGE electrophoresis and sedimentation-velocity analytical ultracentrifugation. The IL-11 Δ_{10} /IL-11Rα $_{D1-D3}$ /gp130 $_{EC}$ complex was prepared using an identical method, although the complex used for cryo-EM was not size exclusion purified, which provided improved particle dispersion.

Cryo-electron microscopy—data collection and 3D reconstruction

Cryo-EM was performed at the Bio21 Institute Ian Holmes Imaging Centre. The IL-11 Δ_{10} /IL-11Rα $_{D1-D3}$ /gp130 $_{D1-D3}$ complex (0.5 mg/mL) was blotted onto UltrAuFoil grids (R2/2, Quantifoil Micro Tools GmbH) that had been subjected to glow discharge (15 mA for 30 s). The sample was applied to the grid at 95% humidity, 4 °C, in a Vitrobot Mark IV (FEI) and blotted for 2 s with a blot force of -1, before plunging in liquid ethane. Grids were imaged using a Gatan K2 direct detector mounted on a

Talos Arctica (FEI, Hillsborough, Oregon) with a 70- μm objective aperture. The detector was operated in super-resolution counting mode at 0.655 $\text{\AA}/\text{pixel}$ (100,000 \times magnification) with a defocus range of -0.8 to -2.0 μm . 40 frames per movie were acquired for a total dose of 50 electrons \AA^{-2} . Movies were acquired with specimen grids at tilts of 0° and 35° to increase particle orientation distribution.

The IL-11 Δ_{10} /IL-11R $\alpha_{\text{D1-D3}}$ /gp130 $_{\text{EC}}$ complex (1.5 mg/mL) in the presence of 1–2 mM *n*-dodecyl β -D-maltoside was blotted onto UltraAuFoil grids (R2/2, Quantifoil Micro Tools GmbH) that had been subjected to glow discharge (15 mA for 30 s). The sample was applied to the grid at 95% humidity, 4 $^\circ\text{C}$, in a VitroBot MarkIV (FEI) and blotted for 2 s with a blot force of -1 , before plunging in liquid ethane. Grids were imaged using a Gatan K2 direct detector mounted on a Talos Arctica (FEI) with a 70- μm objective aperture. The detector was operated in counting mode. The complex was imaged at 1.31 $\text{\AA}/\text{pixel}$ (100,000 \times microscope magnification) with a defocus range of -0.8 to -2.0 μm . 40 frames per movie were acquired for a total dose of 50 electrons \AA^{-2} .

Processing of data for the IL-11 Δ_{10} /IL-11R $\alpha_{\text{D1-D3}}$ /gp130 $_{\text{D1-D3}}$ complex was carried out using RELION-3.0^{82,83} (Supplementary Fig. 1A). Movie motion was corrected using MotionCorr2.1⁸⁴. Cryosparc 2.1⁶³ was used for CTF estimation using the patch CTF estimation routine. A total of 3,082,536 particles were extracted from 2,010 motion-corrected movies. After 2D class averaging in Cryosparc 2.1⁶³, 625,866 particles were retained and were re-extracted in RELION-3.0 with the original defocus from Cryosparc 2.1⁶³. After 3D classification 204,455 particles were used for the final 3D refinement. Final refinement with C2 symmetry yielded a map with a resolution of 3.5 \AA . Resolution was estimated using gold standard FSC = 0.143 calculated using a relaxed solvent map. Maps were sharpened using *phenix.auto_sharpen*⁸⁵. Local resolution maps were calculated using *Resmap*⁸⁶. Buried surface area was determined using *PISA*.

Processing of data for the IL-11 Δ_{10} /IL-11R $\alpha_{\text{D1-D3}}$ /gp130 $_{\text{EC}}$ complex was carried out using Cryosparc 2.1⁶³ (Supplementary Fig. 1B). Movie motion was corrected using MotionCorr2.1⁸⁴. Cryosparc 2.1⁶³ was used for CTF estimation using the patch CTF estimation routine. WARP⁸⁷ was used to pick 694,360 particles from 6,861 motion corrected movies. After 3 rounds of 2D classification, particles were submitted to heterogenous refinement and one further 2D classification leading to a final particle number of 125,373. These particles were used for standard refinement (4.0 \AA) followed by a final non-uniform refinement using C2 symmetry leading to a map with a resolution of 3.8 \AA .

Cryo-electron microscopy—model building and refinement

For the IL-11 Δ_{10} /IL-11R $\alpha_{\text{D1-D3}}$ /gp130 $_{\text{D1-D3}}$ complex, published models of IL-11⁴⁹ (PDB ID: 6O4O), gp130 D1-D3 (chain A from PDB ID: 1IIR³⁴), and the IL-11R α chain from an antibody-bound structure of IL-11R α were docked into the cryo-EM density map of the IL-11 Δ_{10} /IL-11R $\alpha_{\text{D1-D3}}$ /gp130 $_{\text{D1-D3}}$ complex using *UCSF Chimera*⁸⁸ to generate an initial model of the complex. This model was refined using *phenix.real_space_refine*⁸⁹, followed by manual model-building in *Coot*⁹⁰ and automated refinement in *phenix.real_space_refine*. Strict NCS was enforced in refinement. Reference model restraints were used throughout refinement, using the initial models as the reference models.

For the IL-11 Δ_{10} /IL-11R $\alpha_{\text{D1-D3}}$ /gp130 $_{\text{EC}}$ complex, published models of IL-11⁴⁹ (PDB ID: 6O4O), gp130 D1-D3 (chain A from PDB ID: 1IIR³⁴) gp130 $_{\text{D4-D6}}$ ⁵⁸ (PDB ID: 3LS1), and the IL-11R α chain from an antibody-bound structure of IL-11R α were docked into the cryo-EM density map of the IL-11 Δ_{10} /IL-11R $\alpha_{\text{D1-D3}}$ /gp130 $_{\text{D1-D3}}$ complex using *UCSF Chimera*⁸⁸ to generate an initial model of the complex. Refinement was conducted in the same manner as the IL-11 Δ_{10} /IL-11R $\alpha_{\text{D1-D3}}$ /gp130 $_{\text{D1-D3}}$ complex. The deposited model of the IL-11 Δ_{10} /IL-11R $\alpha_{\text{D1-D3}}$ /gp130 $_{\text{EC}}$ complex did not include the D5-D6 domains of gp130; we prepared a second model, which we did not deposit to the PDB, which included

the D5-D6 domains of gp130. This model is included in SASBDB deposition SASDLN3. The structure of IL-11R α used as the initial model for cryo-EM model building is not currently available due to intellectual property considerations. The same analysis of the cryo-EM data can be repeated with the available structure 6O4P⁴⁹.

Geometry validation was performed using the *phenix.validation_cryoem* tool (incorporating *MOLProbity*) and *EMRinger*^{91,92}. Structures were visualised using *UCSF Chimera*⁸⁸. Structures were aligned using the *Matchmaker* algorithm in *UCSF Chimera*⁸⁸ or the *CE* algorithm⁹³ in *PyMOL 2.2*. Map-model FSC curves were calculated in *Phenix*. Figures were prepared using *UCSF Chimera*⁸⁸. The conclusions regarding the binding interactions described are supported by the gp130 $_{\text{D1-D3}}$ and gp130 $_{\text{EC}}$ complex structures, and the crystal structure of the complex. Figure 2 was prepared with the gp130 $_{\text{D1-D3}}$ complex structure, as this structure is supported by the highest resolution data.

For the IL-11 Δ_{10} /IL-11R $\alpha_{\text{D1-D3}}$ /gp130 $_{\text{EC}}$ complex 3D variability analysis with 3 modes to solve was performed in C1 symmetry on the final 125,373 particles used for refinement without symmetry expansion. 3D variability display was used in intermediate mode with 9 frames for each mode solved.

Protein crystallisation and X-ray data collection

The IL-11 complex for crystallisation was prepared by combining equimolar amounts of IL-11 $_{\text{FL}}$, IL-11R α_{EC} and gp130 $_{\text{D1-D3}}$, followed by purification of the complex using gel filtration. Crystals of the IL-11 signalling complex were grown at 20 $^\circ\text{C}$ in 180 mM magnesium chloride, 15.3% PEG 3350, 100 mM potassium sodium tartrate, 90 mM sodium HEPES pH 7.25 and 1.8% tert-butanol. Crystallisation drops were prepared by mixing equal volumes of the precipitant and IL-11 signalling complex (at 3 mg/mL), and 10 μL of a seed stock (prepared according to the method of Luft and DeTitta)⁹⁴. Crystals were flash-cooled in liquid nitrogen directly from crystallisation drops, and X-ray diffraction data were collected at 100 K at the Australian Synchrotron MX2 beamline⁹⁵. X-ray data collection statistics are tabulated in Supplementary Table 2.

Initial crystals of IL-11 Δ_{10} /Mutein were obtained using a similar screening approach to IL-11 Δ_{10} ⁴⁹, in the precipitant 30% PEG 3350, 0.2 M ammonium sulfate, 0.1 M Tris pH 8.5, 20 $^\circ\text{C}$. These initial crystals were used to prepare a microseed stock⁹⁴. Large, single plates of IL-11 Δ_{10} /Mutein grew in the condition 27% PEG 3350, 0.1 M bis-tris propane pH 9, 0.2 M ammonium sulfate, 5 mM praseodymium chloride, 20 $^\circ\text{C}$. Crystallisation drops were produced by mixing 1.5 μL precipitant, 1.5 μL IL-11 Δ_{10} /Mutein (5 mg/mL) and 0.5 μL seed. Crystals of IL-11 Δ_{10} /Mutein were large plates, with approximate dimensions 200 \times 200 \times 5 μm . A similar approach was used to crystallise IL-11 Δ_{10} /W147A. These mutants were cross seeded with seed generated from IL-11 Δ_{10} or IL-11 Δ_{10} /Mutein crystals and grew in very similar conditions to IL-11 Δ_{10} /Mutein. Crystals of IL-11 Δ_{10} /W147A were rods, similar to crystals of IL-11 Δ_{10} ⁴⁹.

Crystals were flash-cooled in liquid nitrogen directly from crystallisation drops, and X-ray diffraction data were collected at 100 K at the Australian Synchrotron MX2 beamline⁹⁵. X-ray data collection statistics are tabulated in Supplementary Table 2.

X-ray data processing and structure refinement

For the IL-11 signalling complex, diffraction data were indexed, integrated and scaled using *XDS*⁹⁶, analysed using *POINTLESS*⁹⁷ and merged using *AIMLESS*⁹⁸ from the *CCP4* suite. Due to the highly anisotropic nature of the data, an ellipsoidal resolution cutoff was applied using the *STARANISO*⁹⁹ server. Initial phase estimates were obtained using molecular replacement with *Phaser*¹⁰⁰ using the cryo-EM structure of the IL-11 Δ_{10} /IL-11R $\alpha_{\text{D1-D3}}$ /gp130 $_{\text{D1-D3}}$ complex as the search model. Refinement was performed in *phenix.refine*¹⁰¹, including several rounds of simulated annealing early in the refinement process. Strict NCS restraints (NCS constraints), reference model restraints using the

high-resolution structures of the complex components, and Ramachandran restraints were employed. Iterative model-building was performed in *Coot*⁹⁰ using NCS-averaged maps. NCS map averaging was performed in *Coot*. N-linked glycans were defined in the electron density and were included in the model. Refinement statistics are tabulated in Supplementary Table 2.

For IL-11 $_{\Delta 10}$ /Mutein^r and IL-11 $_{\Delta 10}$ /W147A^r, diffraction data were indexed, integrated and scaled using *XDS*⁹⁶, analysed using *POINTLESS*⁹⁷ and merged using *AIMLESS*⁹⁸, initial phase estimates were obtained using molecular replacement with *Phaser*¹⁰⁰, using either our original structure of IL-11 (PDB ID: 4MHL)⁸¹ for IL-11 $_{\Delta 10}$ /Mutein or our high-resolution structure of IL-11 $_{\Delta 10}$ for IL-11 $_{\Delta 10}$ /W147A (PDB ID: 6O4O)⁴⁹ as the search model. Auto-building with simulated annealing was performed in *phenix.autobuild* to reduce phase bias from the search model. Refinement was performed in *phenix.refine*¹⁰¹ with iterative manual building using *Coot*⁹⁰. TLS refinement was performed using a single TLS group containing all protein atoms. Explicit riding hydrogens were used throughout refinement and included in the final model, the atomic position and *B* factors for hydrogens were not refined. Residues of all structures are numbered in an identical manner to our structure of IL-11 $_{\Delta 10}$ (PDB ID: 6O4O)⁴⁹, reflecting the mature protein sequence after cleavage of signal peptide. Structures were aligned using the CE⁹³ algorithm in *PyMOL* 2.2. Refinement statistics are tabulated in Supplementary Table 2.

Analytical ultracentrifugation

SV-AUC experiments were conducted using a Beckman Coulter XL-I analytical ultracentrifuge or a Beckman Optima analytical ultracentrifuge, both equipped with UV-visible scanning optics. Samples were loaded into double-sector cells with quartz windows, and centrifuged using an An-60 Ti or An-50 Ti rotor at 50,000 rpm (209,625 *g*) and at 20 °C. Radial absorbance data was collected in continuous mode at 230, 250 or 280 nm. Sedimentation data were fit to a continuous sedimentation coefficient *c*(*s*) model, with floating frictional ratios using *SEDFIT*¹⁰². Buffer density, viscosity and the partial specific volume of the protein samples were calculated using *SEDNTERP*¹⁰³. For complexes, the partial specific volume used was 0.73 mL/*g*.

SE-AUC experiments were conducted using a Beckman Coulter XL-I analytical ultracentrifuge, equipped with UV-visible scanning optics. 160 μ L of sample was loaded into double-sector cells and centrifuged using an An-60 TI rotor. To calculate *M*^{*} for each component of the IL-11 signalling complex, proteins were diluted such that *A*₂₈₀ - 0.35, and then centrifuged sequentially at 10,500 rpm (9,244 *g*), 17,000 rpm (24,232 *g*) and 28,000 rpm (65,738 *g*) until equilibrium was reached. For gp130_{EC}, the three speeds were 8000 rpm (5,366 *g*), 10,000 rpm (8,385 *g*) and 16,000 rpm (21,465 *g*). For the IL-11 $_{\Delta 10}$ /gp130_{D1-D3}/IL-11R $_{\alpha D1-D3}$ complex the complex was diluted such that *A*₂₅₀ - 0.35 and then centrifuged sequentially at 5,300 rpm (2,355 *g*), 6,300 rpm (3,328 *g*) and 9,000 rpm (6,791 *g*). For the IL-11 $_{\Delta 10}$ /gp130_{EC}/IL-11R $_{\alpha D1-D3}$ complex, the three speeds used were 4000 rpm (1,341 *g*), 5000 rpm (2,096 *g*) and 8000 rpm (5,366 *g*). For all samples, *M*^{*} was determined using a single-species analysis model in *SEDPHAT*¹⁰⁴. For the complexes, the sample was size exclusion purified prior to analysis, and sample purity was confirmed with SV-AUC prior to the SE-AUC experiment.

Multi-angle light scattering

SEC-MALS data were collected using a Shimadzu LC-20AD HPLC, coupled to a Shimadzu SPD-20A UV detector, Wyatt Dawn MALS detector and Wyatt Optilab refractive index detector. Data were collected following in-line fractionation with a Zenix-C SEC-300 4.6 \times 300 mm SEC column (Sepax Technologies, cat. 233300-4630), pre-equilibrated in 20 mM Tris, 150 mM sodium chloride pH 8.5, running at a flow rate of 0.35 mL/min. 10 μ L of sample was applied to the column at a concentration of ~2 mg/mL. MALS data were analysed

using ASTRA v.7.3.2.19 (Wyatt). The MALS detector response was normalised using monomeric bovine serum albumin (BSA) (Pierce, cat. 23209). Protein concentration was determined using differential refractive index, using a *dn/dc* of 0.184.

Small-angle X-ray scattering

SAXS experiments were conducted at the Australian Synchrotron SAXS/WAXS beamline¹⁰⁵⁻¹⁰⁷. The X-ray beam energy was 11,500 eV ($\lambda = 1.078$ Å), the sample-to-detector distance is noted in Supplementary Table 3. Data were collected following fractionation with an in-line size-exclusion chromatography column (Superdex 200 5/150 Increase, GE Healthcare, cat. 28990945) pre-equilibrated in TBS pH 8.5, 0.2% sodium azide. Data were reduced and analysed using Scatterbrain, CHROMIXS¹⁰⁸ and ATSAS^{108,109}, data were analysed using CRY SOL and DAMMIF/DAMAVAR/DAMMIN¹¹⁰⁻¹¹². No constant subtraction was applied in CRY SOL. A summary is given in Supplementary Table 3.

Models were prepared of the IL-11 $_{\Delta 10}$ /IL-11R $_{\alpha D1-D3}$ /gp130_{D1-D3} complex, the IL-11 $_{\Delta 10}$ /IL-11R $_{\alpha D1-D3}$ /gp130_{D2-D3} complex, the IL-11 $_{\Delta 10}$ /IL-11R $_{\alpha D1-D3}$ /gp130_{EC} complex, and the IL-11 $_{\Delta 10}$ /Mutein/IL-11R $_{\alpha D1-D3}$ /gp130_{D1-D3} complex based on the IL-11 $_{\Delta 10}$ /IL-11R $_{\alpha D1-D3}$ /gp130_{EC} complex (see Supplementary Table 3 for the regions of the complex used) for fitting to scattering data in CRY SOL. To fit the IL-11 $_{\Delta 10}$ /IL-11R $_{\alpha D1-D3}$ /gp130_{EC} complex data, the model of the gp130_{EC} complex with the D5-D6 domains included was used. For the crystal structure of the IL-11 signalling complex, one hexamer from the crystal structure was used. For IL-11 $_{\Delta 10}$ /Mutein and IL-11 $_{\Delta 10}$ /W147A^r, the unmodified crystal structure coordinates were used.

Multi-state models of the gp130_{EC} complex were generated and fit to the gp130_{EC} complex SAXS data using the Multi-FoXS server¹¹³ (version main.d5bb161). Flexible residues were defined in the IL-11R $_{\alpha D1-D2}$ linker, and the gp130_{EC} D3-D4, D4-D5 and D5-D6 linkers (Supplementary Table 3), the overall complex assembly was defined as a single rigid body, and 10,000 conformations were generated. The gp130_{EC} complex coordinates with D5-D6 domains included was fit to the SAXS data using the FoXS server¹¹⁴ for direct comparison.

Isothermal titration calorimetry

Protein samples were buffer exchanged into TBS pH 8.5 using size exclusion prior to analysis by ITC. ITC data were collected using a MicroCal ITC 200 (GE Healthcare). Titrations were performed using 15 2.5 μ L injections of the cytokine ligand, after an initial injection of 0.8 μ L. IL-11R $_{\alpha D1-D3}$ was present at a concentration of 10 μ M and the concentration of IL-11 or the relevant IL-11 mutant in the syringe was 10-fold greater than the concentration of IL-11R $_{\alpha}$. Following the formation of the cytokine/receptor complex, gp130_{D1-D3} or gp130_{D2-D3} was loaded in the syringe at a concentration 10-fold greater than the concentration of IL-11R $_{\alpha}$ in the cell, a subsequent titration of gp130 against the cytokine/IL-11R $_{\alpha D1-D3}$ complex was then performed at 288 K. Titration data were integrated using *NITPIC*^{115,116}, and analysed in *SEDPHAT*¹¹⁷ using a 1:1 interaction model as defined by the AUC data. Each titration was conducted in triplicate, values stated are the mean \pm standard error of the mean. Significance of differences were calculated using a one-tailed paired *t*-test.

Cell stimulations and phospho-Stat3 flow cytometry assay

Ba/F3 cells stably expressing human gp130 and IL-11R $_{\alpha}$ (generated at WEHI)⁶⁵ were cultured in RPMI-1640 medium containing 10% v/v heat inactivated FBS, 1% v/v Penicillin-Streptomycin and 10 ng/mL recombinant IL-11 $_{\Delta 10}$ at 37 °C and 5% CO₂. Cells were routinely tested for mycoplasma and confirmed to be negative prior to experiments.

Cancer cell lines MDA-MD-231, A549, U87-MG, BxPC3, and LnCap (Cell Bank Australia codes: 92020424, 86012804, 89081402, JCRB1448, 89110211, respectively) were cultured in RPMI-1640 medium containing 10% v/v heat inactivated FBS, 1% v/v Penicillin-Streptomycin, at 37 °C and 5% CO₂, except for MDA-MD-231, which were cultured

in DMEM. Each cell line was routinely tested for mycoplasma and confirmed to be negative prior to experiments.

Cells were seeded at 50,000 cells per well of a 96-well plate overnight and serum starved for 2 h prior to stimulation. To determine EC_{50} , the cells were stimulated with the indicated concentration of IL-11 $_{\Delta 10}$, IL-11 $_{\Delta 10}$ /Mutein, IL-11 $_{\Delta 10}$ /W147A, or IL-11 $_{\Delta 10}$ /PAIDY prepared in Fixable Viability Dye (1/1000, eBioscience Fixable Viability Dye eFluor 506, Thermo Fisher Scientific cat. 65-0866-14) for 15 min at 37 °C. To determine IC_{50} , the cells were incubated with the indicated concentration of IL-11 $_{\Delta 10}$ /Mutein, IL-11 $_{\Delta 10}$ /W147A, or IL-11 $_{\Delta 10}$ /PAIDY for 15 min at 37 °C followed by stimulation with 20 ng/mL IL-11 $_{\Delta 10}$ prepared in Fixable Viability Dye and incubated for a further 15 min at 37 °C.

Cells were harvested by centrifugation at 1600 rpm for 3 min and fixed in Cytofix Fixation Buffer (BD Biosciences, cat. 554655) for 10 min at 37 °C. Cells were then centrifuged and washed with Stain Buffer (BD Biosciences cat. 554656) and permeabilised with Phosphoflow Perm buffer III (BD Biosciences cat. 558050) for 30 min at 40 °C. Cells were then centrifuged, washed with Stain Buffer and stained with Phospho-STAT3 antibody (1/10, clone 4/P-STAT3, BD Biosciences cat. 557815) or Mouse IgG2a, κ Isotype control (1/10, clone MOPC-173 (RUO), BD Biosciences cat. 558053). Data were acquired on a BD Biosciences Fortessa instrument and analysed using FloJo 10.8.2 software. See Supplementary Fig. 9D for gating strategy. EC_{50}/IC_{50} experiments were conducted in triplicate and values are presented as mean \pm standard error of the mean. Statistical analysis was performed in GraphPad Prism 9.4.1.

Molecular dynamics

All MD simulations were performed using NAMD 2.1.3b1¹¹⁸ and the CHARMM22 forcefield^{118,119} at 310 K in a water box with periodic boundary conditions. A model of each of IL-11 $_{\Delta 10}$ and IL-11 $_{\Delta 10}$ /Mutein was built based on the crystal structures, for residues with multiple orientations, only one was selected. The structures were solvated (box size 53.6 \times 53.1 \times 74.9 Å), and ions added to approximate final concentration of 0.15 M NaCl. The MD simulations were performed using 10 ps minimisation time, followed by 1050 ns MD.

Visualisation and analysis was performed in VMD 1.9.3¹²⁰. A script was used in VMD to measure the distance and calculate the distance distribution between T56/S53 O γ and H86 N ϵ throughout the simulation. A script was used to calculate the hydrogen bond potential energy and potential energy distribution of this interaction using a simple electrostatic model, based on the model used in the secondary structure analysis programme DSSP¹²¹. Per-residue C α RMSD and order parameter (S^2) values were calculated using scripts in VMD (available at <https://doi.org/10.5281/zenodo.8302141>).

Differential scanning fluorometry

Protein samples were analysed by DSF at a concentration of 0.1 mg/mL in TBS pH 8 + 0.02% sodium azide, with 2.5 \times SYPRO Orange dye (Sigma Aldrich, cat. S5692). 20 μ L of the sample was loaded into 96-well qPCR plate (Applied Biosystems), and four technical replicates of each sample were analysed. The plates were sealed, and samples heated in an Applied Biosystems StepOne Plus qPCR instrument, from 20 °C to 95 °C, with a 1% gradient. Unfolding data were analysed using a custom script in MATLAB r2019a (available at <https://doi.org/10.5281/zenodo.8302206>). The temperature of hydrophobic exposure (T_h), was defined as the minimum point of the first derivative curve, and used to compare the thermal stability of different proteins⁶⁹. All experiments were repeated three times, values are given as mean \pm standard error of the mean. Significance of differences were calculated using a two-tailed paired t -test.

Surface plasmon resonance

SPR experiments were conducted using a Biacore T200, at 25 °C, in TBS pH 8.5 + 0.05% Tween, running at 30 μ L/min. Experimental conditions and buffer composition were chosen to optimise stability of the

interacting partners while minimising non-specific interactions. Biotinylated IL-11 $_{\Delta 10}$ -avi and IL-11 $_{\Delta 10}$ /Mutein-avi were loaded onto separate channels on a SAHC 1500 M streptavidin chip (Xantec). Both proteins were immobilised until R_{max} was \sim 70. The chip was washed extensively with 1 M NaCl until the baseline was stable. A nine-point, two-fold dilution series of IL-11R α_{D1-D3} was prepared, starting at a concentration of 500 nM. Each IL-11R α dilution was injected over both flow cells in triplicate and reference-subtracted data was generated by subtracting the response from channels in which no protein was loaded from channels containing protein. Data were fit to a 1:1 kinetic model and the Biacore analysis software was used to determine association (k_a) and dissociation (k_d) rates, and the dissociation constant, K_D . Dilution series were prepared and analysed in duplicate, with each complete replicate dilution series analysed separately. Values are given as mean \pm standard error of the mean.

Reporting summary

Further information on research design is available in the Nature Portfolio Reporting Summary linked to this article.

Data availability

Cryo-EM maps generated in this study have been deposited in the Electron Microscopy Data Bank (EMDB) under accession codes EMD-27641 (IL-11 $_{\Delta 10}$ /IL-11R α_{D1-D3} /gp130 $_{D1-D3}$ complex), EMD-27632 (IL-11 $_{\Delta 10}$ /IL-11R α_{D1-D3} /gp130 $_{EC}$ complex). Atomic model coordinates generated in this study have been deposited in the Protein Data Bank (PDB) under accession codes 8DPS (IL-11 $_{\Delta 10}$ /IL-11R α_{D1-D3} /gp130 $_{D1-D3}$ complex), 8DPT (IL-11 $_{\Delta 10}$ /IL-11R α_{D1-D3} /gp130 $_{EC}$ complex). Structure factors and atomic model coordinates generated in this study have been deposited in the PDB under accession codes 8DPU (IL-11 $_{\Delta 10}$ /IL-11R α_{D1-D3} /gp130 $_{D1-D3}$ complex), 8DPV (IL-11 $_{\Delta 10}$ /W147A), 8DPW (IL-11 $_{\Delta 10}$ /Mutein).

Previously published coordinates used in this study are available in the PDB under accession codes 6O4O (IL-11 $_{\Delta 10}$), 11IR (vIL-6 signalling complex), 3L5I (gp130 $_{D4-D6}$), 4MHL (IL-11), 1P9M (IL-6 signalling complex) and 1PVH (LIF/gp130 complex). The structure of IL-11R α used as the initial model for cryo-EM model building is not currently available due to intellectual property considerations. The same analysis of the cryo-EM data can be repeated with the available structure 6O4P.

SAXS data generated in this study and associated atomic model coordinates have been deposited in the Small Angle Scattering Biological Data Bank (SASBDB) with the following accession codes: SASDLM3 (IL-11 $_{\Delta 10}$ /IL-11R α_{D1-D3} /gp130 $_{D1-D3}$ complex), SASDLN3 (IL-11 $_{\Delta 10}$ /IL-11R α_{D1-D3} /gp130 $_{EC}$ complex), SASDLP3 (IL-11 $_{\Delta 10}$ /IL-11R α_{D1-D3} /gp130 $_{D2-D3}$ complex), SASDLS3 (IL-11 $_{\Delta 10}$ /Mutein/IL-11R α_{D1-D3} /gp130 $_{D1-D3}$ complex), SASDLR3 (IL-11 $_{\Delta 10}$ /Mutein), SASDLQ3 (IL-11 $_{\Delta 10}$ /W147A).

Molecular dynamics protein structure files (PSF) and trajectories have been deposited on Figshare at <https://doi.org/10.6084/m9.figshare.24043518> (IL-11 $_{\Delta 10}$ microsecond MD trajectory) and <https://doi.org/10.6084/m9.figshare.24043527> (IL-11 $_{\Delta 10}$ /Mutein microsecond MD trajectory). Source data for the ITC data presented in Figs. 2, 5 and 6 was deposited on Figshare at <https://doi.org/10.6084/m9.figshare.24293080>. Source data for the SPR data presented in Fig. 5D was deposited on Figshare at <https://doi.org/10.6084/m9.figshare.24293563>.

Other data are contained within the manuscript and Supplementary Information. Materials generated in this study may be obtained from the corresponding author for non-commercial research use via a materials transfer agreement. Source data are provided with this paper.

Code availability

VMD scripts used for analysis of the MD trajectories are available on Zendo at <https://doi.org/10.5281/zenodo.8302141>. The MATLAB script used for DSF data analysis is available on Zendo at <https://doi.org/10.5281/zenodo.8302206>.

References

1. Anderson, K. C. et al. Interleukin-11 promotes accessory cell-dependent B-cell differentiation in humans. *Blood* **80**, 2797–2804 (1992).
2. Curti, A. et al. Interleukin-11 induces Th2 polarization of human CD4(+) T cells. *Blood* **97**, 2758–2763 (2001).
3. Zhang, X. et al. IL-11 induces Th17 cell responses in patients with early relapsing-remitting multiple sclerosis. *J. Immunol.* **194**, 5139–5149 (2015).
4. Elshabrawy, H. A. et al. IL-11 facilitates a novel connection between RA joint fibroblasts and endothelial cells. *Angiogenesis* **21**, 215–228 (2018).
5. Huynh, J. et al. Host IL11 signaling suppresses CD4(+) T cell-mediated antitumor responses to colon cancer in mice. *Cancer Immunol. Res* **9**, 735–747 (2021).
6. Nayar, S. et al. A myeloid-stromal niche and gp130 rescue in NOD2-driven Crohn's disease. *Nature* **593**, 275–281 (2021).
7. Minshall, E. et al. IL-11 expression is increased in severe asthma: association with epithelial cells and eosinophils. *J. Allergy Clin. Immunol.* **105**, 232–238 (2000).
8. Calon, A. et al. Dependency of colorectal cancer on a TGF-beta-driven program in stromal cells for metastasis initiation. *Cancer Cell* **22**, 571–584 (2012).
9. Ng, B. et al. Interleukin-11 is a therapeutic target in idiopathic pulmonary fibrosis. *Sci. Transl. Med.* **11**, 12–37 (2019).
10. Schafer, S. et al. IL-11 is a crucial determinant of cardiovascular fibrosis. *Nature* **552**, 110–115 (2017).
11. Widjaja, A. A. et al. Inhibiting interleukin 11 signaling reduces hepatocyte death and liver fibrosis, inflammation, and steatosis in mouse models of nonalcoholic steatohepatitis. *Gastroenterology* **157**, 777–792.e714 (2019).
12. Paul, S. R. et al. Molecular cloning of a cDNA encoding interleukin 11, a stromal cell-derived lymphopoietic and hematopoietic cytokine. *Proc. Natl Acad. Sci.* **87**, 7512–7516 (1990).
13. Metcalfe, R., Putoczki, T. & Griffin, M. Structural understanding of interleukin 6 family cytokine signaling and targeted therapies: focus on interleukin 11. *Front. Immunol.* **11**, 1–25 (2020).
14. Wu, S. et al. Multicenter, randomized study of genetically modified recombinant human interleukin-11 to prevent chemotherapy-induced thrombocytopenia in cancer patients receiving chemotherapy. *Support Care Cancer* **20**, 1875–1884 (2012).
15. Okamoto, H. et al. The synovial expression and serum levels of interleukin-6, interleukin-11, leukemia inhibitory factor, and oncostatin M in rheumatoid arthritis. *Arthritis Rheum.* **40**, 1096–1105 (1997).
16. Adami, E. et al. IL11 is elevated in systemic sclerosis and IL11-dependent ERK signalling underlies TGFbeta-mediated activation of dermal fibroblasts. *Rheumatol.* **60**, 5820–5826 (2021).
17. Strikoudis, A. et al. Modeling of fibrotic lung disease using 3D organoids derived from human pluripotent stem cells. *Cell Rep.* **27**, 3709–3723 (2019).
18. Corden, B., Adami, E., Sweeney, M., Schafer, S. & Cook, S. A. IL-11 in cardiac and renal fibrosis: late to the party but a central player. *Br. J. Pharm.* **177**, 1695–1708 (2020).
19. Corden, B. et al. Therapeutic targeting of interleukin-11 signalling reduces pressure overload-induced cardiac fibrosis in mice. *J. Cardiovasc. Transl. Res.* **14**, 222–228 (2021).
20. Widjaja, A. A. et al. A neutralizing IL-11 antibody improves renal function and increases lifespan in a mouse model of Alport Syndrome. *J. Am. Soc. Nephrol.* **33**, 718–730 (2022).
21. van Duijneveldt, G., Griffin, M. D. W. & Putoczki, T. L. Emerging roles for the IL-6 family of cytokines in pancreatic cancer. *Clin. Sci.* **134**, 2091–2115 (2020).
22. Liang, M. et al. IL-11 is essential in promoting osteolysis in breast cancer bone metastasis via RANKL-independent activation of osteoclastogenesis. *Cell Death Dis.* **10**, 353 (2019).
23. Ernst, M. et al. STAT3 and STAT1 mediate IL-11-dependent and inflammation-associated gastric tumorigenesis in gp130 receptor mutant mice. *J. Clin. Invest* **118**, 1727–1738 (2008).
24. Putoczki, T. L. et al. Interleukin-11 is the dominant IL-6 family cytokine during gastrointestinal tumorigenesis and can be targeted therapeutically. *Cancer Cell* **24**, 257–271 (2013).
25. Lay, V., Yap, J., Sonderegger, S. & Dimitriadis, E. Interleukin 11 regulates endometrial cancer cell adhesion and migration via STAT3. *Int. J. Oncol.* **41**, 759–764 (2012).
26. Barton, V., Hall, M., Hudson, K. R. & Heath, J. K. Interleukin-11 signals through the formation of a hexameric receptor complex. *J. Biol. Chem.* **275**, 36197–36203 (2000).
27. Morris, R., Kershaw, N. J. & Babon, J. J. The molecular details of cytokine signaling via the JAK/STAT pathway. *Protein Sci.* **27**, 1984–2009 (2018).
28. Mahboubi, K., Biedermann, B. C., Carroll, J. M. & Pober, J. S. IL-11 activates human endothelial cells to resist immune-mediated injury. *J. Immunol.* **164**, 3837–3846 (2000).
29. Thiem, S. et al. mTORC1 inhibition restricts inflammation-associated gastrointestinal tumorigenesis in mice. *J. Clin. Invest* **123**, 767–781 (2013).
30. Derouet, D. et al. Neuropeptin, a new IL-6-related cytokine signaling through the ciliary neurotrophic factor receptor. *Proc. Natl Acad. Sci. USA* **101**, 4827–4832 (2004).
31. Murakami, M., Kamimura, D. & Hirano, T. New IL-6 (gp130) family cytokine members, CLC/NNT1/BSF3 and IL-27. *Growth Factors* **22**, 75–77 (2004).
32. Rose-John S. Interleukin-6 family cytokines. *Cold Spring Harb. Perspect Biol.* **10**, a028415 (2018).
33. Tait Wojno, E. D., Hunter, C. A. & Stumhofer, J. S. The immunobiology of the interleukin-12 family: room for discovery. *Immunity* **50**, 851–870 (2019).
34. Chow, D.-C., He, X., Snow, A. L., Rose-John, S. & Garcia, K. Structure of an extracellular gp130 cytokine receptor signaling complex. *Science* **291**, 2150–2155 (2001).
35. Boulanger, M. J., Chow, D.-C., Brevnova, E. E. & Garcia, K. C. Hexameric structure and assembly of the interleukin-6/IL-6 alpha-receptor/gp130 complex. *Science* **300**, 2101–2104 (2003).
36. Huyton, T. et al. An unusual cytokine:Ig-domain interaction revealed in the crystal structure of leukemia inhibitory factor (LIF) in complex with the LIF receptor. *Proc. Natl Acad. Sci.* **104**, 12737–12742 (2007).
37. Boulanger, M. J., Bankovich, A. J., Kortemme, T., Baker, D. & Garcia, K. C. Convergent mechanisms for recognition of divergent cytokines by the shared signaling receptor gp130. *Mol. Cell* **12**, 577–589 (2003).
38. Caveney N. A., Glassman C. R., Jude K. M., Tsutsumi N., Garcia K. C. Structure of the IL-27 quaternary receptor signaling complex. *Elife* <https://doi.org/10.7554/eLife.78463> (2022).
39. Jin, Y. et al. Structural insights into the assembly and activation of the IL-27 signaling complex. *EMBO Rep.* **23**, e55450 (2022).
40. Zhou, Y. et al. Structural insights into the assembly of gp130 family cytokine signaling complexes. *Sci. Adv.* **9**, eade4395 (2023).
41. Wong, P. K., Campbell, I. K., Robb, L. & Wicks, I. P. Endogenous IL-11 is pro-inflammatory in acute methylated bovine serum albumin/interleukin-1-induced (mBSA/IL-1)arthritis. *Cytokine* **29**, 72–76 (2005).
42. Schumacher, D. et al. A neutralizing IL-11 antibody reduces vessel hyperplasia in a mouse carotid artery wire injury model. *Sci. Rep.* **11**, 20674 (2021).

43. Lee, C. G. et al. Endogenous IL-11 signaling is essential in Th2- and IL-13-induced inflammation and mucus production. *Am. J. Respir. Cell Mol. Biol.* **39**, 739–746 (2008).
44. Underhill-Day, N. et al. Functional characterization of W147A: A high-affinity interleukin-11 antagonist. *Endocrinology* **144**, 3406–3414 (2003).
45. Wu, P. et al. IL-11 is elevated and drives the profibrotic phenotype transition of orbital fibroblasts in thyroid-associated ophthalmopathy. *Front. Endocrinol.* **13**, 846106 (2022).
46. Winship, A. L., Van Sinderen, M., Donoghue, J., Rainczuk, K. & Dimitriadis, E. Targeting interleukin-11 receptor- α impairs human endometrial cancer cell proliferation and invasion in vitro and reduces tumor growth and metastasis in vivo. *Mol. Cancer Therapeut.* **15**, 720–730 (2016).
47. Ng B., et al. IL11 activates pancreatic stellate cells and causes pancreatic inflammation, fibrosis and atrophy in a mouse model of pancreatitis. *Int. J. Mol. Sci.* **23**, 3549 (2022).
48. Lim, W. W. et al. Inhibition of IL11 signaling reduces aortic pathology in Murine Marfan Syndrome. *Circ. Res.* **130**, 728–740 (2022).
49. Metcalfe, R. D. et al. The structure of the extracellular domains of human interleukin 11 α receptor reveals mechanisms of cytokine engagement. *J. Biol. Chem.* **295**, 8285–8301 (2020).
50. Matadeen, R., Hon, W. C., Heath, J. K., Jones, E. Y. & Fuller, S. The dynamics of signal triggering in a gp130-receptor complex. *Structure* **15**, 441–448 (2007).
51. Skiniotis, G., Boulanger, M. J., Garcia, K. C. & Walz, T. Signaling conformations of the tall cytokine receptor gp130 when in complex with IL-6 and IL-6 receptor. *Nat. Struct. Mol. Biol.* **12**, 545–551 (2005).
52. Lupardus, P. J. et al. Structural snapshots of full-length Jak1, a transmembrane gp130/IL-6/IL-6R α cytokine receptor complex, and the receptor-Jak1 holocomplex. *Structure* **19**, 45–55 (2011).
53. Barton, V., Hudson, K. R. & Heath, J. K. Identification of three distinct receptor binding sites of murine interleukin-11. *J. Biol. Chem.* **274**, 5755–5761 (1999).
54. Tacke, I. et al. Definition of receptor binding sites on human interleukin-11 by molecular modeling-guided mutagenesis. *Eur. J. Biochem.* **265**, 645–655 (1999).
55. Czupryn, M. et al. Alanine-scanning mutagenesis of human interleukin-11: identification of regions important for biological activity. *Ann. N. Y. Acad. Sci.* **762**, 152–164 (1995).
56. Kurth, I. et al. Activation of the signal transducer glycoprotein 130 by both IL-6 and IL-11 requires two distinct binding epitopes. *J. Immunol.* **162**, 1480–1487 (1999).
57. Li, H. & Nicholas, J. Identification of amino acid residues of gp130 signal transducer and gp80 α receptor subunit that are involved in ligand binding and signaling by human herpesvirus 8-encoded interleukin-6. *J. Virol.* **76**, 5627–5636 (2002).
58. Xu, Y. et al. Crystal structure of the entire ectodomain of gp130: insights into the molecular assembly of the tall cytokine receptor complexes. *J. Biol. Chem.* **285**, 21214–21218 (2010).
59. Skiniotis, G., Lupardus, P. J., Martick, M., Walz, T. & Garcia, K. C. Structural organization of a full-length gp130/LIF-R cytokine receptor transmembrane complex. *Mol. Cell* **31**, 737–748 (2008).
60. Timmermann, A., Küster, A., Kurth, I., Heinrich, P. C. & Müller-Newen, G. A functional role of the membrane-proximal extracellular domains of the signal transducer gp130 in heterodimerization with the leukemia inhibitory factor receptor. *Eur. J. Biochem.* **269**, 2716–2726 (2002).
61. Kurth, I. et al. Importance of the membrane-proximal extracellular domains for activation of the signal transducer glycoprotein 130. *J. Immunol.* **164**, 273–282 (2000).
62. Punjani, A. & Fleet, D. J. 3D variability analysis: Resolving continuous flexibility and discrete heterogeneity from single particle cryo-EM. *J. Struct. Biol.* **213**, 107702 (2021).
63. Punjani, A., Rubinstein, J. L., Fleet, D. J. & Brubaker, M. A. CryoSPARC: Algorithms for rapid unsupervised cryo-EM structure determination. *Nat. Methods* **14**, 290–296 (2017).
64. Chen, Y. H. et al. Functional and structural analysis of cytokine-selective IL6ST defects that cause recessive hyper-IgE syndrome. *J. Allergy Clin. Immunol.* **148**, 585–598 (2021).
65. Nandurkar, H. H. et al. The human IL-11 receptor requires gp130 for signalling: demonstration by molecular cloning of the receptor. *Oncogene* **12**, 585–593 (1996).
66. Shepelkova, G., Evstifeev, V., Majorov, K., Bocharova, I. & Apt, A. Therapeutic effect of recombinant mutated interleukin 11 in the mouse model of tuberculosis. *J. Infect. Dis.* **214**, 496–501 (2016).
67. Wang, H., Wang, D. H., Yang, X., Sun, Y. & Yang, C. S. Colitis-induced IL11 promotes colon carcinogenesis. *Carcinogenesis* **42**, 557–569 (2021).
68. Ashraf, S. S., Benson, R. E., Payne, E. S., Halbleib, C. M. & Grøn, H. A novel multi-affinity tag system to produce high levels of soluble and biotinylated proteins in *Escherichia coli*. *Protein Expr. Purif.* **33**, 238–245 (2004).
69. Seabrook, S. A. & Newman, J. High-throughput thermal scanning for protein stability: making a good technique more robust. *ACS Comb. Sci.* **15**, 387–392 (2013).
70. Zhou, Y. et al. Structural insights into the assembly of gp130 family cytokine signaling complexes. *bioRxiv* <https://doi.org/10.1101/2022.06.30.496838> (2022).
71. Widjaja, A. A. et al. Molecular dissection of pro-fibrotic IL11 signaling in cardiac and pulmonary fibroblasts. *Front. Mol. Biosci.* **8**, 740650 (2021).
72. Chen, Y. H. et al. Absence of GP130 cytokine receptor signaling causes extended Stüve-Wiedemann syndrome. *J. Exp. Med.* **217**, e20191306 (2020).
73. Beziat, V. et al. Dominant-negative mutations in human IL6ST underlie hyper-IgE syndrome. *J. Exp. Med.* **217**, e20191804 (2020).
74. Shahin, T. et al. Selective loss of function variants in IL6ST cause hyper-IgE syndrome with distinct impairments of T-cell phenotype and function. *Haematologica* **104**, 609–621 (2019).
75. Schwerd, T. et al. A biallelic mutation in IL6ST encoding the GP130 coreceptor causes immunodeficiency and craniosynostosis. *J. Exp. Med.* **214**, 2547–2562 (2017).
76. Monies, D. et al. Lessons learned from large-scale, first-tier clinical exome sequencing in a highly consanguineous population. *Am. J. Hum. Genet.* **104**, 1182–1201 (2019).
77. Schwerd, T. et al. A variant in IL6ST with a selective IL-11 signaling defect in human and mouse. *Bone Res.* **8**, 24 (2020).
78. Nieminen, P. et al. Inactivation of IL11 signaling causes craniosynostosis, delayed tooth eruption, and supernumerary teeth. *Am. J. Hum. Genet.* **89**, 67–81 (2011).
79. Neveling, K. et al. Mutations in the interleukin receptor IL11RA cause autosomal recessive Crozon-like craniosynostosis. *Mol. Genet. Genom. Med.* **1**, 223–237 (2013).
80. Klein, W. et al. A promotor polymorphism in the Interleukin 11 gene is associated with chronic obstructive pulmonary disease. *Electrophoresis* **25**, 804–808 (2004).
81. Putoczki, T. L., Dobson, R. C. J. & Griffin, M. D. W. The structure of human interleukin-11 reveals receptor-binding site features and structural differences from interleukin-6. *Acta. Crystallogr. Sect. D.-Biol. Crystallogr.* **3**, 2277–2285 (2014).
82. Kimanius, D., Forsberg, B. O., Scheres, S. H., & Lindahl, E. Accelerated cryo-EM structure determination with parallelisation using GPUs in RELION-2. *Elife* <https://doi.org/10.7554/eLife.18722> (2016).

83. Scheres, S. H. Semi-automated selection of cryo-EM particles in RELION-1.3. *J. Struct. Biol.* **189**, 114–122 (2015).
84. Zheng, S. Q. et al. MotionCor2: anisotropic correction of beam-induced motion for improved cryo-electron microscopy. *Nat. Methods* **14**, 331–332 (2017).
85. Terwilliger, T. C., Sobolev, O. V., Afonine, P. V. & Adams, P. D. Automated map sharpening by maximization of detail and connectivity. *Acta. Crystallogr. Sect. D. Struct. Biol.* **74**, 545–559 (2018).
86. Kucukelbir, A., Sigworth, F. J. & Tagare, H. D. Quantifying the local resolution of cryo-EM density maps. *Nat. Methods* **11**, 63–65 (2014).
87. Tegunov, D. & Cramer, P. Real-time cryo-electron microscopy data preprocessing with Warp. *Nat. Methods* **16**, 1146–1152 (2019).
88. Pettersen, E. F. et al. UCSF Chimera—a visualization system for exploratory research and analysis. *J. Comput. Chem.* **25**, 1605–1612 (2004).
89. Afonine, P. V. et al. Real-space refinement in phenix for cryo-EM and crystallography. *Acta. Crystallogr. Sect. D. Struct. Biol.* **74**, 531–544 (2018).
90. Emsley, P., Lohkamp, B., Scott, W. G. & Cowtan, K. Features and development of coot. *Acta. Crystallogr. Sect. D. Biol. Crystallogr.* **66**, 486–501 (2010).
91. Barad, B. A. et al. EMRinger: side chain-directed model and map validation for 3D cryo-electron microscopy. *Nat. Methods* **12**, 943–946 (2015).
92. Williams, C. J. et al. MolProbity: More and better reference data for improved all-atom structure validation. *Protein Sci.* **27**, 293–315 (2018).
93. Shindyalov, I. N. & Bourne, P. E. Protein structure alignment by incremental combinatorial extension (CE) of the optimal path. *Protein Eng.* **11**, 739–747 (1998).
94. Luft, J. R. & DeTitta, G. T. A method to produce microseed stock for use in the crystallization of biological macromolecules. *Acta. Crystallogr. Sect. D: Biol. Crystallogr.* **55**, 988–993 (1999).
95. Aragão, D. et al. MX2: a high-flux undulator microfocussing beamline serving both the chemical and macromolecular crystallography communities at the Australian Synchrotron. *J. Synchrotron. Radiat.* **25**, 885–891 (2018).
96. Kabsch, W. Xds. *Acta. Crystallogr. Sect. D: Biol. Crystallogr.* **66**, 125–132 (2010).
97. Evans, P. Scaling and assessment of data quality. *Acta. Crystallogr. Sect. D: Biol. Crystallogr.* **62**, 72–82 (2006).
98. Evans, P. R. & Murshudov, G. N. How good are my data and what is the resolution? *Acta. Crystallogr. Sect. D: Biol. Crystallogr.* **69**, 1204–1214 (2013).
99. Tickle, I. J. et al. STARANISO. <http://staraniso.globalphasing.org/cgi-bin/staraniso.cgi> (2018).
100. McCoy, A. J. et al. Phaser crystallographic software. *J. Appl. Crystallogr.* **40**, 658–674 (2007).
101. Afonine, P. V. et al. Towards automated crystallographic structure refinement with phenix.refine. *Acta. Crystallogr. Sect. D: Biol. Crystallogr.* **68**, 352–367 (2012).
102. Schuck, P. Size-distribution analysis of macromolecules by sedimentation velocity ultracentrifugation and lamm equation modeling. *Biophys. J.* **78**, 1606–1619 (2000).
103. Laue T. M., Shah B. D., Ridgeway T. M., Pelletier S. L. *Analytical Ultracentrifugation in Biochemistry and Polymer Science*. (Cambridge Royal Society of Chemistry, 1992).
104. Vistica, J. et al. Sedimentation equilibrium analysis of protein interactions with global implicit mass conservation constraints and systematic noise decomposition. *Anal. Biochem.* **326**, 234–256 (2004).
105. Kirby, N. M. et al. A low-background-intensity focusing small-angle X-ray scattering undulator beamline. *J. Appl. Crystallogr.* **46**, 1670–1680 (2013).
106. Kirby, N. et al. Improved radiation dose efficiency in solution SAXS using a sheath flow sample environment. *Acta Crystallogr. Sect. D. Struct. Biol.* **72**, 1254–1266 (2016).
107. Ryan, T. M. et al. An optimized SEC-SAXS system enabling high X-ray dose for rapid SAXS assessment with correlated UV measurements for biomolecular structure analysis. *J. Appl. Crystallogr.* **51**, 97–111 (2018).
108. Panjkovich, A. & Svergun, D. I. CHROMIXS: automatic and interactive analysis of chromatography-coupled small-angle X-ray scattering data. *Bioinformatics* **34**, 1944–1946 (2017).
109. Franke, D. et al. ATSAS 2.8: A comprehensive data analysis suite for small-angle scattering from macromolecular solutions. *J. Appl. Crystallogr.* **50**, 1212–1225 (2017).
110. Franke, D. & Svergun, D. I. DAMMIF, a program for rapid ab-initio shape determination in small-angle scattering. *J. Appl. Crystallogr.* **42**, 342–346 (2009).
111. Volkov, V. V. & Svergun, D. I. Uniqueness of ab initio shape determination in small-angle scattering. *J. Appl. Crystallogr.* **36**, 860–864 (2003).
112. Svergun, D. Restoring low resolution structure of biological macromolecules from solution scattering using simulated annealing. *Biophys. J.* **76**, 2879–2886 (1999).
113. Schneidman-Duhovny, D., Hammel, M., Tainer, J. A. & Sali, A. FoXS, FoXSDock and MultiFoXS: single-state and multi-state structural modeling of proteins and their complexes based on SAXS profiles. *Nucleic Acids Res.* **44**, W424–W429 (2016).
114. Schneidman-Duhovny, D., Hammel, M., Tainer, J. A. & Sali, A. Accurate SAXS profile computation and its assessment by contrast variation experiments. *Biophys. J.* **105**, 962–974 (2013).
115. Brautigam, C. A., Zhao, H., Vargas, C., Keller, S. & Schuck, P. Integration and global analysis of isothermal titration calorimetry data for studying macromolecular interactions. *Nat. Protoc.* **11**, 882–894 (2016).
116. Keller, S. et al. High-precision isothermal titration calorimetry with automated peak shape analysis. *Anal. Chem.* **84**, 5066–5073 (2012).
117. Zhao, H. & Schuck, P. Combining biophysical methods for the analysis of protein complex stoichiometry and affinity in SEDPHAT. *Acta. Crystallogr. Sect. D Biol. Crystallogr.* **71**, 3–14 (2015).
118. Phillips, J. C. et al. Scalable molecular dynamics with NAMD. *J. Comput. Chem.* **26**, 1781–1802 (2005).
119. Brooks, B. R. et al. CHARMM: The biomolecular simulation program. *J. Comput. Chem.* **20**, 1545–1614 (2009).
120. Humphrey, W., Dalke, A. & Schulten, K. VMD: Visual molecular dynamics. *J. Mol. Graph.* **7855**, 33–38 (1996).
121. Kabsch, W. & Sander, C. Dictionary of protein secondary structure: pattern recognition of hydrogen-bonded and geometrical features. *Biopolymers* **22**, 2578–2637 (1983).

Acknowledgements

Parts of this research were conducted at the SAXS/WAXS and MX2 beamlines of the Australian Synchrotron, part of the Australian Nuclear Science and Technology Organisation, and made use of the ACRF Detector at the MX2 beamline. Initial crystallisation screens were conducted at the CSIRO Collaborative Crystallisation Centre, Melbourne, Australia. This research made use of the ACRF Facility for Innovative Cancer Drug Discovery and the LIEF HPC-GPGPU Facility hosted at the University of Melbourne (LE170100200). We acknowledge the Ian Holmes Imaging Centre, the Melbourne Protein Characterisation Platform, and the Melbourne Mass Spectrometry and Proteomics Facility, at the Bio21 Molecular Science and Biotechnology Institute, for exceptional technical support. This work was supported by the National Health & Medical Research Council of Australia (APP1147621, APP1080498 to M.D.W.G. and T.L.P.), Cancer Council New South Wales (RG 22-01 to

M.D.W.G. and T.L.P.), and the Australian Research Council (DP230102422 to M.D.W.G. and T.L.P.). R.D.M. was the recipient of an Australian Government Research Training Program Scholarship. M.W.P. is an NHMRC Investigator Fellow (APP1194263). T.L.P. is the recipient of a Sylvia and Charles Viertel Senior Medical Research Fellowship. Funding from the Victorian State Government Operational Infrastructure Support Scheme is acknowledged.

Author contributions

R.D.M., E.H., T.L.P., and M.D.W.G. conceived the studies, designed and performed experiments, analysed data, and wrote the manuscript. K.Y.F., K.A., C.O.Z., C.C.K., L.D., C.J.M., and A.P.L. designed and performed experiments, and analysed data. M.W.P. and P.R.G. contributed critical resources and intellectual input. All authors have read and agreed to the manuscript content.

Competing interests

T.L.P. has consulted for enterprises involved in biological drug development (Mestag Therapeutics, Enleofen Ltd). M.D.W.G. has consulted for enterprises involved in biological drug development (Mestag Therapeutics). T.L.P. and M.D.W.G. are founders of Nelcanen Therapeutics Pty Ltd. Other authors declare that they have no conflicts of interest.

Additional information

Supplementary information The online version contains supplementary material available at <https://doi.org/10.1038/s41467-023-42754-w>.

Correspondence and requests for materials should be addressed to Michael D. W. Griffin.

Peer review information *Nature Communications* thanks Savvas Savvides, Stephen Muench, Mikhail Kutuzov and Michal Hammel for their contribution to the peer review of this work.

Reprints and permissions information is available at <http://www.nature.com/reprints>

Publisher's note Springer Nature remains neutral with regard to jurisdictional claims in published maps and institutional affiliations.

Open Access This article is licensed under a Creative Commons Attribution 4.0 International License, which permits use, sharing, adaptation, distribution and reproduction in any medium or format, as long as you give appropriate credit to the original author(s) and the source, provide a link to the Creative Commons licence, and indicate if changes were made. The images or other third party material in this article are included in the article's Creative Commons licence, unless indicated otherwise in a credit line to the material. If material is not included in the article's Creative Commons licence and your intended use is not permitted by statutory regulation or exceeds the permitted use, you will need to obtain permission directly from the copyright holder. To view a copy of this licence, visit <http://creativecommons.org/licenses/by/4.0/>.

© The Author(s) 2023